CHEMISTRY
A European Journal

A Journal of
ChemPubSoc Europe

Accepted Article

Title: A spectroscopic and computationally minimal approach to the analysis of charge transfer processes in conformationally fluxional mixed-valence and hetero-bimetallic complexes

Authors: Paul J. Low, Simon Gückel, Josef B. G. Gluyas, Samantha G. Eaves, Parvin Safari, Dmitry S. Yufit, Alexandre N. Sobolev, and Martin Kaupp

To be cited as: *Chem. Eur. J.* 10.1002/chem.201901200

Link to VoR: http://dx.doi.org/10.1002/chem.201901200

Supported by
ACES

WILEY-VCH

10.1002/chem.201901200

A spectroscopic and computationally minimal approach to the analysis of charge transfer processes in conformationally fluxional mixed-valence and hetero-bimetallic complexes

Simon Gückel,[a] Josef B. G. Gluyas,[b] Samantha G. Eaves,[b,c] Parvin Safari,[b] Dmitry S. Yufit,[c] Alexandre N. Sobolev,[b] Martin Kaupp,[a]* Paul J. Low[b]*

[a] Technische Universität Berlin, Institut für Chemie, Theoretische Chemie/Quantenchemie, Sekr. C7, Strasse des 17. Juni 135, 10623 Berlin, Germany

[b] School of Molecular Sciences, University of Western Australia, 35 Stirling Highway, Crawley 6009, Western Australia, Australia

[c] Department of Chemistry, Durham University, South Road, Durham, DH1 3LE, UK

* Corresponding Authors: MK: martin.kaupp@tu-berlin.de (t) +49 30 314 79682. PJL: paul.low@uwa.edu.au (t) +61 (08) 6488 3045

Supporting information for this article is available on the WWW under http://dx.doi.org/10.1002/chem.2018xxxxx.

Abstract

The Class II mixed-valence bimetallic complexes {[Cp'(PP)M]C≡C–C≡N[M'(PP)'Cp']}$^{2+}$ (M, M' = Ru, Fe; PP = dppe, $(PPh_3)_2$; Cp' = Cp*, Cp) exist as conformational ensembles in fluid solution, with a population of structures ranging from *cis*-like to *trans*-like geometries. Each conformer gives rise to its own series of low energy IVCT and local dd transitions which overlap in the NIR region, giving complex band envelopes in the NIR absorption spectrum which prevent any meaningful attempt at analysis of the band-shape. However, DFT and TDDFT calculations with dispersion-corrected global hybrid (BLYP35-D3) or local-hybrid (lh-SsirPW92-D3) functionals on a small number of optimised structures chosen to sample the ground state potential energy hypersurfaces of each of these complexes has proven sufficient to explain the major features of the electronic spectra. Although modest in terms of computational expense, this approach provides a more accurate description of the underlying molecular electronic structure than would be possible through analysis of the intervalence charge transfer (IVCT)

band using the static point-charge model of Marcus-Hush theory and derivatives, or (TD-)DFT calculations from a single (global) minimum energy geometry.

Introduction

Mixed-valence complexes of general form [E(μ-bridge)E]$^{\pm}$, in which some element or redox-active molecular fragment (E) is present in more than one formal oxidation or charge state, have faithfully served as systems through which to explore intramolecular charge transfer processes, and from which in turn theoretical models of increasing sophistication have been developed.[1] Whilst organic mixed-valence systems are known,[2] metal complex based mixed valence complexes of general form [{L_nM}(μ-bridge){ML_n}]$^{\pm}$ (M = metal, L_n = ancillary ligand sphere) are by far more common.[1g, 3] Information concerning the electronic structure of such systems is commonly inferred from the metal-to-metal (or intervalence) charge transfer electronic transition (IVCT), with the band shape and energy analysed within the framework of Marcus-Hush theory. At its heart, Marcus-Hush theory begins with an approximation of mixed-valence compounds, and donor-acceptor compounds more generally, in terms of weakly coupled point charges separated by a well-defined distance over which charge transfer occurs.[1g, 4] As the Marcus-Hush two-state model provides a number of convenient relationships through which to extract electronic information from experimentally observable features of the IVCT band, it has become established as the most commonly employed framework through which to carry out analysis of the electronic properties of mixed-valence complexes. In addition, the Robin-Day classification scheme[5] provides a simple lexicon with which to describe mixed-valence compounds in terms of the extent of electronic coupling between the remote, redox-active sites (Class I – no interaction between the redox sites; Class II – weak to moderate interaction between the redox sites; Class III – strong interaction / delocalisation between the redox sites). Whilst heterometallic complexes [{L_nM}(μ-bridge){M'L'_n}]$^{\pm}$ and related asymmetric compounds are not true 'mixed' valence complexes, the term is often also applied in such cases,[6] and the methods of analysis of the metal-to-metal charge transfer transition are closely related to those employed for the IVCT bands of 'asymmetric' homometallic MV complexes, [{L_nM}(μ-bridge){ML'_n}]$^{\pm}$.[2]

Analyses using Marcus-Hush and related theories, and descriptions of mixed-valence complexes drawn from the Robin-Day classification scheme, are all based upon an assumption that the system in question can be described in terms of a single (lowest energy) molecular

structure. However, it is now recognised that the electronic signatures of mixed-valence complexes are complicated by the presence of other low-lying electronic transitions, such as inter-configurational transitions, that can overlap with the IVCT band. In addition, as the symmetry of the ML_n fragment is lowered, the degeneracy of metal d-orbitals is lifted giving rise to the potential for multiple transitions with IVCT character, which can become particularly prominent in metal complexes based on heavier metals in which spin-orbit coupling is pronounced.[3d] Further complications arise in cases where weak coupling and valence localisation results in the 'true' IVCT band being exceptionally weak, broad and low in energy, and hence easily overlooked.[7]

Recently, we have explored the spectroscopic properties and electronic structures of the all-carbon bridged 'Class III' mixed-valence complex $[\{Ru(dppe)Cp^*\}_2(\mu\text{-}C{\equiv}C\text{-}C{\equiv}C)]^+$, and closely related compounds, in some detail.[8] These studies have shown that, in addition to the complications noted above, the population of a number of spectroscopically distinct conformational minima contribute to the convoluted band envelopes observed in the NIR spectra of such complexes. In the case of half-sandwich ruthenium-based butadiyndiyl (C≡C–C≡C) bridged complexes, the metal 4d and carbon chain π orbitals are extensively mixed, giving rise to a highly delocalised electronic structure. As is well known, the low energy electronic transitions in complexes with delocalised electronic structures are better described as charge resonance or π-π* transitions than charge-transfer bands.[9] However, the low energy band envelope also contains a MLCT transition, which gains intensity as the orientation of the cyclopentadienyl rings deviate from *cis*- or *trans*-like orientation.[8a, 8c] The high degree of steric and electronic entanglement between the half-sandwich ligand spheres in $[\{Ru(dppe)Cp^*\}_2(\mu\text{-}C{\equiv}C\text{-}C{\equiv}C)]^+$ results in a restriction of the rotational freedom about the Ru–C≡C–C≡C–Ru axis. In addition, dispersion forces between the dppe ligands give an energetic favouring towards structures in which the half-sandwich fragments adopt relative positions with roughly perpendicular (*perp*) orientations of the pentamethylcyclopentadienyl rings.[8a] Together, these factors increase the prominence of the MLCT component of the NIR band envelope when compared with complexes in which the metal end caps are tethered together and restricted to more *cis*-like geometries. These factors, not known at the time of the original reports,[9] make it clear that the presence of multiple transitions in the band envelope arising from multiple, spectroscopically distinct molecular structures equilibrated

within the sample solution essentially prohibit extraction of accurate parameters using the Marcus-Hush model.

In order to better describe the electronic structures of such conformational ensembles and better explain the features of the NIR band envelope in mixed valence complexes, including a more accurate assessment of the IVCT band, attention was turned to DFT methods using functionals such as BLYP35.[10] The BLYP35 functional is a global hybrid based on B88 exchange and LYP correlation (BLYP functional) using 35% exact-exchange admixture and identified previously as being well suited to analysis of charge-transfer processes.[10b, 11] In the example of $[\{Ru(dppe)Cp^*\}_2(\mu\text{-}C{\equiv}C\text{-}C{\equiv}C)]^+$, a relaxed scan in which partial structure optimisations were carried out with a fixed P–Ru–Ru–P angle in 10° steps ($0 \leq \Omega \leq 180°$) was performed allowing mapping of section of the potential energy hypersurface.[8a] Following this process, local minima were identified, and further unconstrained optimisations performed before the spectral properties of the true minima were examined quantum chemically.

In the case of the more localised (Class II) iron-based examples (e.g. $[\{Fe(dppe)Cp'\}_2(\mu\text{-}C{\equiv}C\text{-}C{\equiv}C)]^+$; Cp' = Cp, Cp*), whilst structure models were successfully obtained using the same protocol, appreciable spin contamination and poor reproduction of the excitation energies was observed using BLYP35-based calculations. Therefore, additional single-point calculations of ground-state energies and TDDFT calculations of excitation spectra were carried out using the local hybrid functional (lh-SsirPW92),[12] with position-dependent exact-exchange admixture and a partially self-interaction-corrected correlation part.[7a] This greatly improved the results for the localised mixed-valence examples whilst returning results entirely consistent with the BLYP35 results in the case of the more delocalized ruthenium systems.

The description of mixed-valence complexes in terms of the ensemble of minima identified from this systematic approach to exploring the ground state hypersurface provides very detailed information for a given compound, and a much more precise description of the electronic structure than is possible from conventional interpretations based on a single molecular structure. However, such fine-grained exploration of the potential energy hypersurface quickly becomes computationally expensive, especially for 'real' systems with

full structural representations of the auxiliary ligands. In order to develop a more readily applied protocol that still provides detailed information concerning the electronic structures of mixed-valence complexes and the features of experimental spectra, we have begun to explore interpretations based on a smaller range of structures chosen to sample the key areas of the hypersurface.

Here, attention is turned to a family of model complexes featuring the cyanoacetylide bridging ligand, [{Cp*(dppe)Ru}(μ-C≡C–C≡N){M(PP)Cp'}]$^+$ ([**1**]$^+$) and [{Cp(dppe)Fe}(μ-C≡C–C≡N){M(PP)Cp'}]$^+$ ([**2**]$^+$) ({M(PP)Cp'} = Ru(dppe)Cp* (**a**), Ru(dppe)Cp (**b**), Ru(PPh_3)$_2$Cp (**c**), Fe(dppe)Cp* (**d**), Fe(dppe)Cp (**e**)). The cyanoacetylide ligand allows the facile, systematic variation of both the metal and the supporting ligand groups at either end of the bridge, giving convenient access to this family of complexes, which includes the non-interconverting linkage isomers [**1e**]$^+$ and [**2a**]$^+$. Bimetallic, cyanoacetylide-bridged complexes generally give rise to well-behaved electrochemical response,[13] making them amenable to study by spectroelectrochemical methods.[14] The half-sandwich fragments are free to rotate around the M-C and N-M' bonds in the same manner as observed for buta-1,3-diyn-1,4-diyl complexes, giving rise to the same conformational complications identified in the earlier studies noted above, and their putative mixed-valence derivatives [**1a – e**]$^{2+}$ and [**2a – e**]$^{2+}$ obtained by one-electron oxidation within a spectroelectrochemical cell are consequently characterised by a series of intense, but poorly resolved, NIR absorption bands. Together, these synthetic, redox and spectroscopic features make the complexes [**1a – e**]$^{n+}$ and [**2a – e**]$^{n+}$ (n = 1, 2) ideal test objects through which to develop a user-friendly approach to the analysis and description of mixed-valence complexes with low axial symmetry and conformationally flexibility.

In the discussion that follows, we demonstrate that a coarse grained computational model, using as few as three distinct molecular structures to sample the key regions of the conformational population, is sufficient to describe the electronic character and account for the appearance of the charge transfer band envelopes observed in the NIR region of asymmetric homometallic mixed valence and heterobimetallic complexes [**1a – e**]$^{2+}$ and [**2a – e**]$^{2+}$. For reasons of computational expense, structure optimisations at the BLYP35-D3/def2-SVP/COSMO(CH_2Cl_2) level were used to identify minima that sample regions of the conformational space in which the Cp(*) rings are located approximately *cis*, *trans* or

perpendicular (*perp*) to each other. TDDFT calculations were carried out on each of these minima using a local hybrid functional (lh-SsirPW92-D3/def2-SVP-COSMO(CH_2Cl_2) level) to alleviate issues with spin contamination in the iron-containing members of the series, and combined to give quite satisfactory models of the experimentally observed band envelopes. Although modest in computational expense, this coarse grained model provides a more detailed interpretation of the charge transfer (or IVCT) bands in these ligand bridged bimetallic (mixed-valence) complexes than can be achieved using the analytical expressions derived from a point-charge model and Marcus-Hush theory, or from single-point TDDFT calculations.

Results and Discussion

Syntheses, Characterisation and Molecular Structures

The readily prepared cyanoacetylide complexes Ru(C≡CC≡N)(dppe)Cp*[13b] and Fe(C≡CC≡N)(dppe)Cp[13a] react with the half-sandwich complexes RuCl(dppe)Cp*, RuCl(dppe)Cp, RuCl(PPh_3)$_2$Cp, FeCl(dppe)Cp* and FeCl(dppe)Cp[15] in the presence of NH_4PF_6 to give cationic, bimetallic complexes [{Cp*(dppe)Ru}(μ-C≡C–C≡N){M(PP)Cp'}]PF_6 ([**1**]PF_6) and [{Cp(dppe)Fe}(μ-C≡C–C≡N){M(PP)Cp'}]PF_6 ([**2**]PF_6) ({M(PP)Cp'} = Ru(dppe)Cp* (**a**), Ru(dppe)Cp (**b**), Ru(PPh_3)$_2$Cp (**c**), Fe(dppe)Cp* (**d**), Fe(dppe)Cp (**e**)) (Scheme 1); compounds [**1a**]PF_6,[13b], [**1c**]PF_6[13b] and [**2c**]PF_6[13a] have been previously reported, and structurally characterised. Each of the new compounds described here have been characterised by standard ^{1}H, ^{13}C and ^{31}P NMR spectroscopic, mass spectrometric, and elemental analytical techniques and single-crystal X-ray diffraction studies. Key metric parameters are summarised in Table 1, and a plot of the cation [**1e**]$^+$ is shown in Figure 1 by way of example; while plots of the other cations are given in Figure S1.

The general structural features of the [{Cp'(PP)M}(μ-C≡CC≡N){M'(PP)'Cp'}]$^+$ cations and comparisons of the bond lengths along the M-C≡CC≡N-M chain with those of the mononuclear fragments have been made elsewhere.[13] However, given the important role that different molecular conformations play in the distribution of electronic structures and spectroscopic properties of closely related buta-1,3-diyn-1,4-diyl complexes,[7a, 8a, 8c] for the purposes of the present investigation it is pertinent to note the torsion angles Ω = Cp$^{\#}$-M...M-Cp'$^{\#}$ (Cp$^{\#}$ = Cp centroid). The cations [**1a**]$^+$, [**1b**]$^+$, [**1d**]$^+$, [**1e**]$^+$ and [**2b**]$^+$ all exhibit torsion angles Ω close to 90°, described as perpendicular (*perp*) conformations, to reduce steric interactions between

10.1002/chem.201901200

the M(dppe)Cp' fragments. In contrast, the Ru(dppe)Cp* and $Ru(PPh_3)_2Cp$ moieties in [**1c**]$^+$ are found in a more *cis*-like conformation (Ω = -17.5$_0$°), whist the introduction of the even smaller Fe(dppe)Cp fragment in [**2c**]$^+$ gives a structure in which the metal fragments are disordered over *cis* (Ω = -12.96°) and *trans* (Ω = 158.8$_5$°) conformations. In the case of [**2e**]$^+$, the two Fe(dppe)Cp moieties are disposed with Ω = -48.7$_0$°, whilst the analogous angles in [**2a**]$^+$ (-66.2$_1$°) and [**2d**]$^+$ (-64.0$_0$°) also fall between the idealised *cis*- and *perp*- conformations.

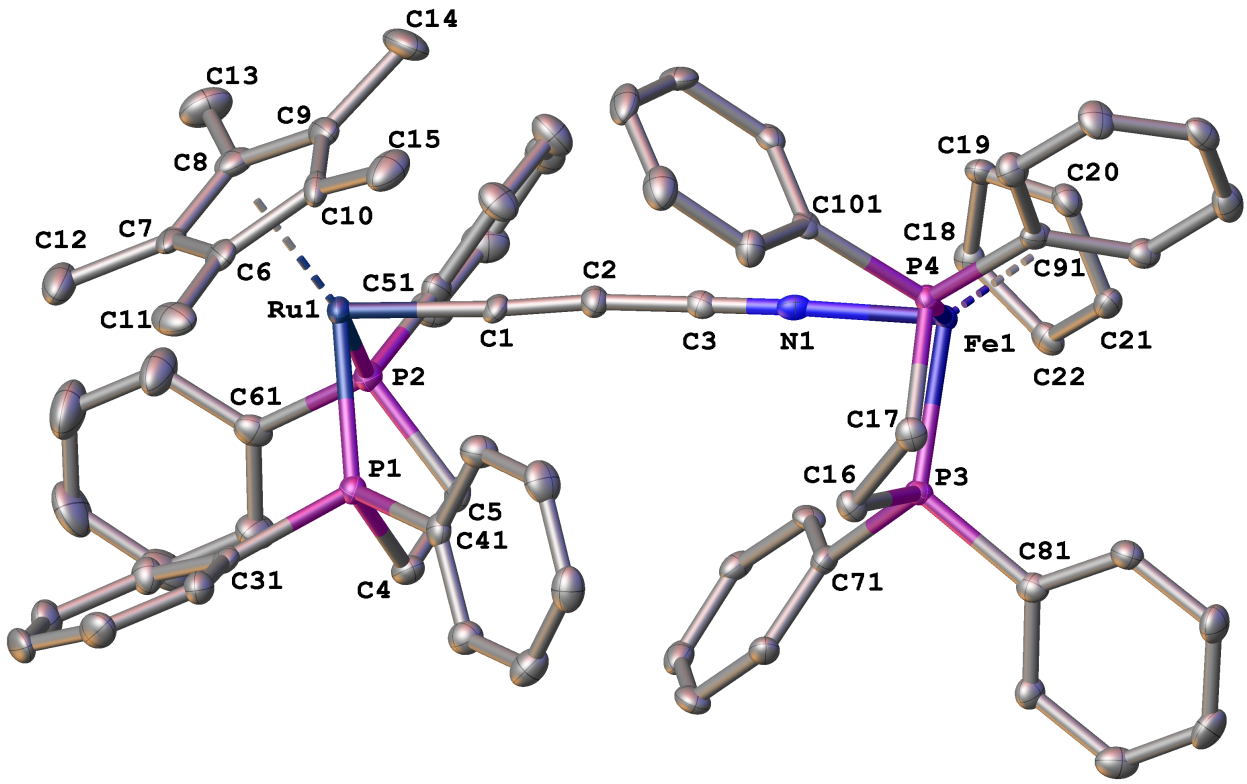

Figure 1. Plot of the cation from the structure of [**1e**]$PF_6 \cdot CH_2Cl_2$. Thermal ellipsoids are plotted at 50% probability. Solvent of crystallisation, the PF_6^- anion and hydrogen atoms have been excluded for clarity.

10.1002/chem.201901200

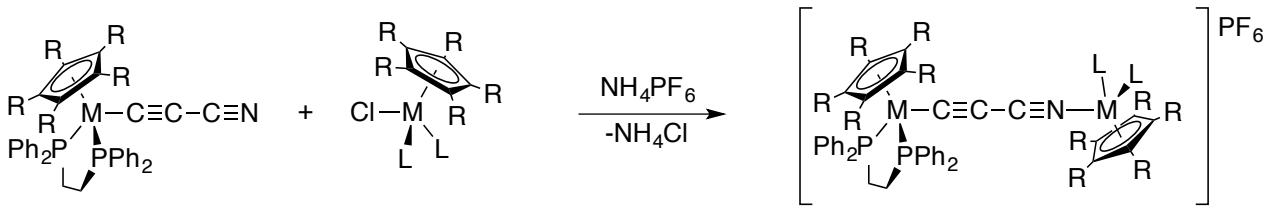

[**1a**]PF_6 [**2a**]PF_6

[**1b**]PF_6 [**2b**]PF_6

[**1c**]PF_6 [**2c**]PF_6

[**1d**]PF_6 [**2d**]PF_6

[**1e**]PF_6 [**2e**]PF_6

Scheme 1. Synthesis of the cyanoacetylide complexes [**1a-e**]PF_6 and [**2a - e**]PF_6.

10.1002/chem.201901200

Table 1. Selected crystallographically determined bond lengths and Cp#-M...M'-Cp'# torsion angles.

[{Cp*(dppe)Ru}(μ-C≡CC≡N){M(PP)Cp'}]+								
M(PP)Cp'	Compound Number	Ω / °	M1–C1	C1-C2	C2-C3	C3-N	N-M2	ref
Ru(dppe)Cp*	[**1a**]+	79.0_6	1.996(3)	1.193(4)	1.354(4)	1.180(4)	2.003(3)	[13b]
Ru(dppe)Cp	[**1b**]+	88.6_1	1.946(4)	1.224(6)	1.356(6)	1.160(5)	2.012(3)	this work
$Ru(PPh_3)_2Cp$	[**1c**]+	-17.5_0	1.944(3)	1.240(4)	1.357(4)	1.154(4)	2.044(2)	[13b]
Fe(dppe)Cp*	[**1d**]+	-83.9_1	1.927(1)	1.224(2)	1.348(2)	1.180(2)	1.895(1)	this work
Fe(dppe)Cp	[**1e**]+	-88.6_5	1.936(4)	1.238(6)	1.353(6)	1.170(5)	1.887(4)	this work
[{Cp(dppe)Fe}(μ-C≡CC≡N){M(PP)Cp'}]+								
M(PP)Cp'	Compound Number	Ω / °	M1–C1	C1-C2	C2-C3	C3-N	N-M2	ref
Ru(dppe)Cp*	[**2a**]+	-66.2_1	1.822(2)	1.249(2)	1.350(2)	1.163(2)	2.020(1)	this work
Ru(dppe)Cp	[**2b**]+	-95.8_3	1.850(4)	1.233(5)	1.342(5)	1.162(5)	2.008(3)	this work
$Ru(PPh_3)_2Cp$	*cis*-[**2c**]+	-12.9_6	1.864(10)	1.217(14)	1.370(13)	1.183(10)	2.056(4)	[13a]
$Ru(PPh_3)_2Cp$	*trans*-[**2c**]+	158.8_5	1.849(7)	1.237(10)	1.374(10)	1.184(8)	2.056(4)	[13a]
Fe(dppe)Cp*	[**2d**]+	-64.0_0	1.839(2)	1.236(3)	1.354(3)	1.161(2)	1.887(2)	this work
Fe(dppe)Cp	[**2e**]+	-48.7_0	1.867(3)	1.202(4)	1.352(4)	1.198(4)	1.873(3)	this work

When examined by cyclic voltammetry, each complex [**1a – e**]PF_6 and [**2a – e**]PF_6 undergoes two or three, presumably 1-electron, oxidation processes (0.1 M NBu_4PF_6 / CH_2Cl_2), separated by 0.40 – 0.79 V, within the electrochemical window (Table 2). The second process shows signs of chemical irreversibility at slower scan rates in some cases (Figure S21) whilst the third is irreversible. The separation of the first and second redox processes gives rise to a large comproportion constant, K_c, which reflects the thermodynamic stability of the one-electron redox products with respect to disproportionation.[16] In this study, attention will be restricted to these thermodynamically and chemically stable, one-electron oxidation products of [**1a – e**]PF_6 and [**2a – e**]PF_6. Note that due to the presence of the nitrogen atom in the bridging ligand, the 35-electron bimetallic mixed-valence complexes generated by one-electron oxidation, [**1a – e**]$^{2+}$ and [**2a – e**]$^{2+}$, bear a dicationic charge.

10.1002/chem.201901200

Table 2. Cyclic voltammetry data from [**1a - e**]$^{+}$ and [**2a – e**]$^{+}$ recorded in CH_2Cl_2 / 0.1 M nBu$_4$NPF$_6$.

	$E_{1/2}(1)$[a]	$E_{1/2}(2)$	$E_p(3)$	$\Delta E_{1\text{-}2}$	$K_{C(1\text{-}2)}$[b]
1a	0.30	0.73	1.15	0.43	1.8×10^7
1b	0.35	0.75	1.23	0.40	5.8×10^6
1c	0.37	0.84	1.00	0.47	8.8×10^7
1d	0.03	0.82	1.17	0.79	2.2×10^{13}
1e	0.12	0.60		0.48	1.3×10^8
2a	0.16	0.67		0.51	4.2×10^8
2b	0.19	0.77	1.39	0.58	6.4×10^9
2c	0.18	0.90	1.41	0.72	1.5×10^{12}
2d	–0.16	0.43		0.59	9.4×10^9
2e	0.09	0.54	1.44	0.45	4.0×10^7

[a] Potentials referenced relative to the decamethylferrocene/decamethylferrocinium couple at –0.48 V (ferrocene/ferrocinium = 0.00 V).[17]

[b] $K_{c(1\text{-}2)} = \exp\{\Delta E/RT\}$

NIR spectroscopy, conformational sampling and TDDFT calculations

The homobimetallic, mixed valence complex [**1a**]$^{2+}$ provides a convenient object through which to demonstrate the proposed method of analysis. The NIR spectrum of [**1a**]$^{2+}$, obtained spectroelectrochemically[14] from a 0.1M NBu_4PF_6 / CH_2Cl_2 solution of [**1a**]PF_6, features two pronounced maxima near 6000 and 8500 cm^{-1} with shoulders to the high and low energy sides of the band envelope (Figure 2). In earlier studies this band was deconvoluted into three Gaussian-shaped sub-bands,[13b] which were attributed to the three primary IVCT-type bands expected of a d^5-d^6 mixed-valence complex featuring pseudo-octahedral metal fragments.[3d]

10.1002/chem.201901200

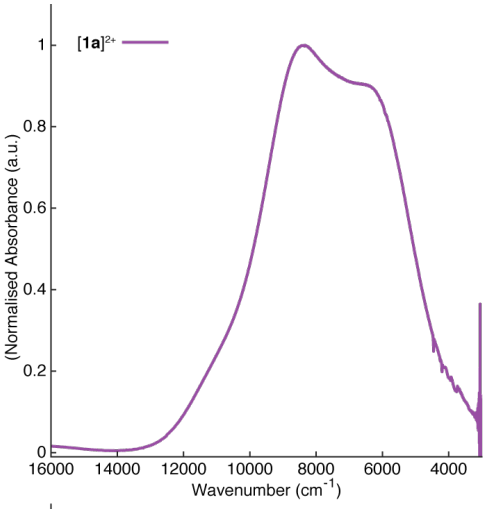

Figure 2. NIR spectra of [**1a**]$^{2+}$ recorded spectroelectrochemically in CH_2Cl_2 / 0.1 M nBu$_4$NPF$_6$.

The identification of the contributions of a conformational distribution to the appearance of the NIR spectra in closely related buta-1,3-diyn-1,4-diyl complexes[8a, 8c] prompts a re-examination of the NIR spectrum of [**1a**]$^{2+}$. We have previously used a fine-grained, systematic approach to search for minima from across the ground state potential energy surfaces of [{Ru(dppe)Cp*}$_2$(μ-C≡C-C≡C)]$^+$, which is structurally related to [**1a** – **e**]$^{2+}$ and [**2a** – **e**]$^{2+}$, and similar mixed-valence complexes. Together with DFT-based descriptions of the electronic structures of these minima, a superposition of TDDFT calculations from each minimum can then be used assist in interpretations of the experimental NIR spectral envelope, the details of which are reported elsewhere.[8] To reduce the computational effort and test a more 'user friendly' methodology, rather than a systematic fine-grained search, here initial starting structures for the optimisations of [**1a**]$^{2+}$ were simply chosen to sample a range of likely rotational orientations of the Cp* rings from the most *cis*-like and most *trans*-like structures, and structures in which the Cp* ligands are approximately perpendicular (*perp*), consistent with the range of solid state structures summarised in Table 1. Unconstrained optimisation of these starting structures (BLYP35-D3/def2-SVP/COSMO) afforded several minima (Ω = 40, 49, 68, and 138 °) that lie within 20 kJ mol^{-1} (Table 3; see Table S1 for structures optimised at this level for [**1a** – **e**]$^{2+}$ and [**2a** – **e**]$^{2+}$). Essentially the same structures were obtained for [**1a**]$^{2+}$ [**1d**]$^{2+}$ and [**2d**]$^{2+}$, chosen as representative examples of homometallic Ru, heterometallic Ru/Fe and homometallic Fe complexes, from structure optimisations carried out at the B3LYP-D3/def2-SVP-COSMO(CH_2Cl_2) level of theory

10.1002/chem.201901200

(Table S2). We note that the use of dispersion corrections proved important in accounting for non-covalent interactions between the ligand spheres; for example, the lowest energy rotational conformer of [**1a**]$^{2+}$ (Ω = 68 °) is stabilised by non-covalent intramolecular interactions between the two half-sandwich ligand spheres.

TDDFT calculations were carried out on each of these minima using the local hybrid functional (lh-SsirPW92), in anticipation of spin contamination problems at BLYP35 level with the iron containing members of the series to follow (vide infra). From the global minimum structure of [**1a**]$^{2+}$ (Ω = 68 °), TDDFT calculations gave a series of excitations which, after application of a line broadening routine to the stick spectrum, result in only modest agreement with the experimental spectrum at best (Figure 3a, Table 3; see Figure S2 and Tables S3,S4 in Supporting Information for results at other computational levels). A very low energy transition at 3265 cm^{-1} likely captures the low energy shoulder which tails into the mid-IR region, whilst two energetically similar transitions at 6846 and 7521 cm^{-1} apparently contribute to the principal, lower energy component of the band envelope. Higher energy excitations at 10201 and 12148 cm^{-1} give rise to features that could perhaps be associated with the higher energy maximum and shoulder in the experimental spectrum.

10.1002/chem.201901200

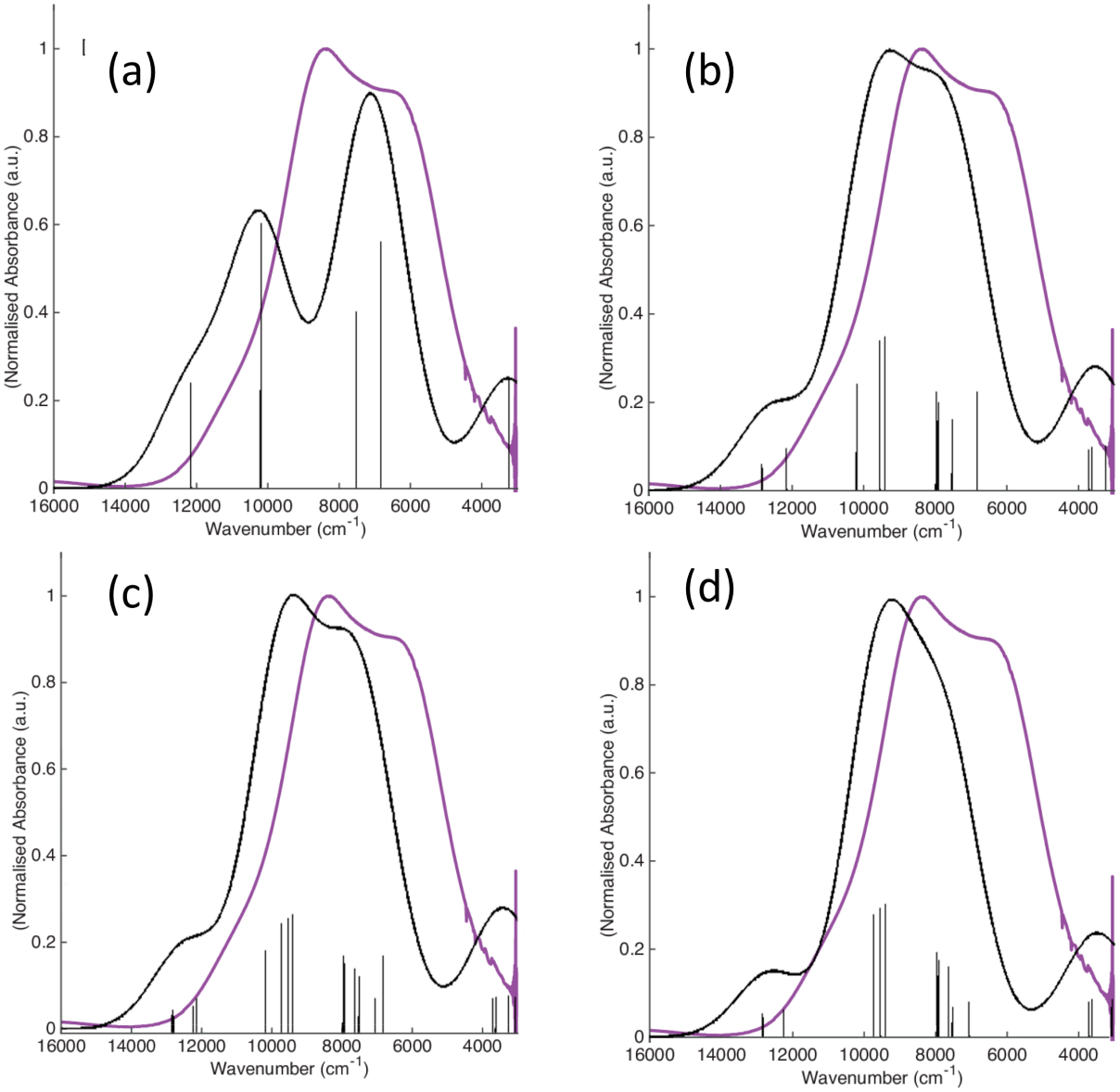

Figure 3. Overlay plot of the experimentally determined NIR spectrum of [**1a**]$^{2+}$ with the normalised, line-broadened (900 cm^{-1}) stick spectrum from TDDFT calculations (lh-SsirPW92-D3/def2-SVP-COSMO(CH_2Cl_2)//BLYP35-D3/def2-SVP-COSMO(CH_2Cl_2)) from: (a) the lowest energy optimised structure (Ω = 68 °); (b) three minima (Ω = 40°, 68°, 138°); (c) four minima (Ω = 40°, 49°, 68°, 138°); (d) three minima (Ω = 40°, 49°, 138°) but without the minimum energy structure (Ω = 68°).

However, by simply summing the TDDFT results from just three minima chosen to represent the *cis* (Ω = 40°, ΔE = +12.1 kJ mol^{-1}) and *trans* (Ω =138°, ΔE = +17.7 kJ mol^{-1}) conformations as well as the *perp*-like global minimum (Ω =68°), a remarkably good agreement between the

10.1002/chem.201901200

line broadened stick spectrum, albeit somewhat blue shifted, and the experimental data was obtained, even without Boltzmann weighting of the sub-spectra (Figure 3b, Table 3). Further inclusion of the fourth minimum (Ω = 49°, ΔE = +3.8 kJ mol^{-1}) resulted in little further improvement in the overall appearance of the computed spectrum (Figure 3c, Table 3). Thus, consideration of only three low-lying minima, sampled from distinct geometric regions of the potential energy surface, is sufficient to give quite an accurate description of the experimental spectrum. However, failure to include the lowest energy minimum in the sample geometries gave rather less good agreement (Figure 3d).

Similar conformer sampling routines were also undertaken for the further examples of homobimetallic ruthenium complexes [**1b**]$^{2+}$ and [**1c**]$^{2+}$. Thus, from initial starting structures selected to sample the *cis*-, *perp*- and *trans*-conformer spaces, a small number of representative minima were identified (Table 3). In each case, as noted above for [**1a**]$^{2+}$, the agreement of the line broadened stick spectrum from TDDFT calculations from only the lowest energy conformation of each compound gave merely the most general agreement with the experimental line-shape (Figure S3, Figure S4). However, the inclusion of additional TDDFT results from a small number of other low-lying minima selected to sample the range of accessible geometries gave substantial improvement (Figure 4).

10.1002/chem.201901200

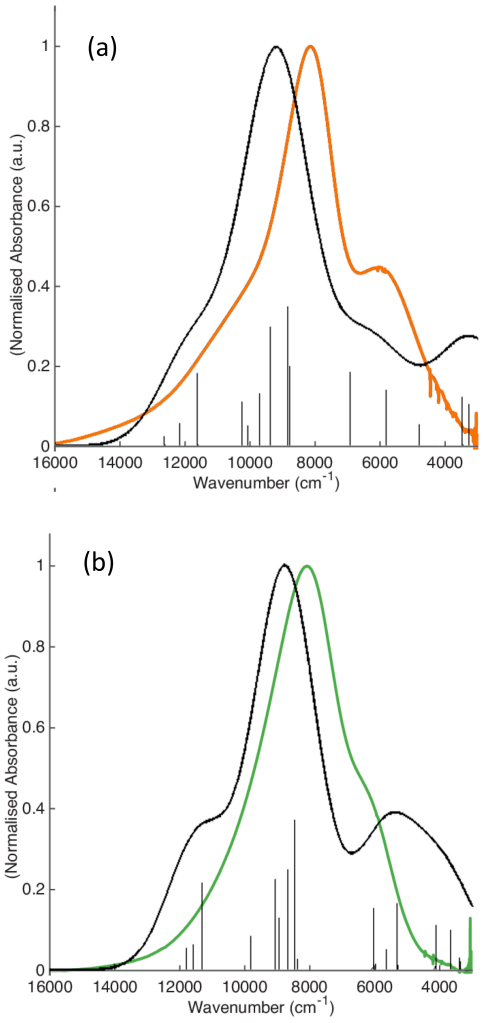

Figure 4. Overlay plot of the experimentally determined NIR spectra of (a) [**1b**]$^{2+}$ (orange trace) and (b) [**1c**]$^{2+}$ (green trace) with the normalised, line-broadened (900 cm^{-1}) stick spectra composed from results of TDDFT calculations (lh-SsirPW92-D3/def2-SVP-COSMO(CH_2Cl_2)//BLYP35-D3/def2-SVP-COSMO(CH_2Cl_2)) with three representative minima in each case ([**1b**]$^{2+}$ Ω = 50°, 69°, 132°); [**1c**]$^{2+}$ Ω = 4°, 78°, 158°) (black traces).

Turning attention to the heterobimetallic complexes [{Cp*(dppe)Ru}(μ-C≡CC≡CN{Fe(dppe)Cp']$^{2+}$ (Cp' = Cp*, [**1d**]$^{2+}$; Cp' = Cp, [**1e**]$^{2+}$), [{Cp(dppe)Fe}(μ-C≡CC≡N){Ru(dppe)Cp'}]$^{2+}$ (Cp' = Cp*, [**2a**]$^{2+}$; Cp' = Cp, [**2b**]$^{2+}$) and [{Cp(dppe)Fe}(μ-C≡CC≡N){Ru(PPh_3)$_2$Cp}]$^{2+}$ ([**2c**]$^{2+}$), the same process of identifying representative minima that sample the key regions of the conformational space was adopted (Table 3). By way of example, the overlay of the experimental and computed spectra are shown for [**1d**]$^{2+}$ in Figure 5, and are given in Supporting Information for the other complexes (Figures S5 – S7).

10.1002/chem.201901200

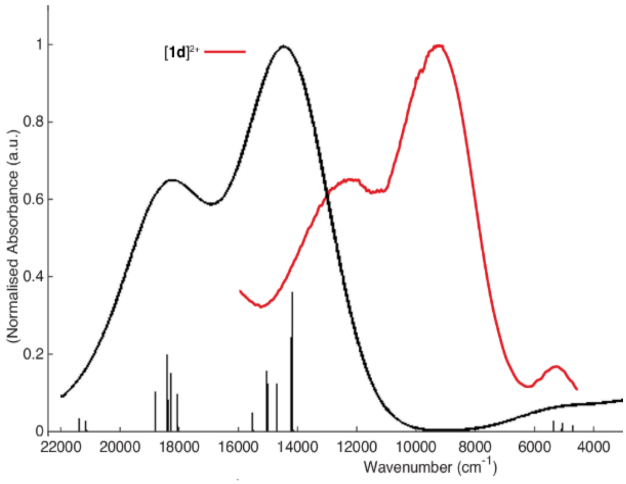

Figure 5. Overlay plot of the experimentally determined NIR spectra of [**1d**]$^{2+}$ (red trace) with the normalised, line-broadened (900 cm^{-1}) stick spectrum composed from TDDFT calculations (lh-SsirPW92-D3/def2-SVP-COSMO(CH_2Cl_2)//BLYP35-D3/def2-SVP-COSMO(CH_2Cl_2)) with three representative minima ([**1d**]$^{2+}$ Ω = 52°, 87°, 143°) (black trace).

The simulated spectra composed from TDDFT calculations with the three representative minimum geometries of heterobimetallic [**1d**]$^{2+}$ (Ω = 52°, 87°, 143°; Figure 5) and [**1e**]$^{+}$ (Ω = 51°, 85°, 134°; Figure S5) and the homobimetallic iron complexes [**2d**]$^{2+}$ (Ω = 46°, 94°, 130°; Figure S9) and [**2e**]$^{2+}$ (Ω = 70°, 82°, 180°; Figure 6) reproduce the main features of the experimental band-shape quite well (cf. Figures S6-S8 for similar overlay plots for **[2a-c]**$^{2+}$). However, the calculated transition energies from the heterobimetallic Ru/Fe and homobimetallic Fe/Fe systems are more blue-shifted than those of the homobimetallic Ru/Ru analogues. These blue-shifts seem to be correlated with the slightly higher S^2 expectation values associated with the more localized Fe(III) character of the iron-containing complexes (Table 3). This spin contamination is even more significant in the BLYP35-D3 calculations of electronic structure of these complexes (S^2 = 0.82 – 0.88), and unsurprisingly the TDDFT results at the BLYP35-D3/def2-SVP-COSMO(CH_2Cl_2) level of theory show even greater shifts from the experimental spectra and fail to adequately model the shape of the experimental band-envelope (c.f. Figure S10). Further sample calculations at B3LYP-D3 level also resulted in poorer agreement than found for the local-hybrid based calculations (Figure S10). Whilst we cannot give a detailed account of the origin of blue-shift in these calculated transition energies, the spin contamination seems to relate to static correlation effects, which are more

10.1002/chem.201901200

pronounced around 3d than 4d (or 5d) centres. This static correlation, which relates to the compact nature of the 3d shell and the severe bond-stretching that arises from Pauli repulsion between the 3p semi-core shell and adjacent ligand orbitals,[18] presents a challenge for current approximate DFT variants that might be overcome in future through more sophisticated functionals, e.g. considering a local mixing of range-separated exchange energy densities. However, at this point in time we can note that the local hybrid functional is a significant improvement over B3LYP and BLYP35 calculations for the present complexes with the most localized electronic structure. Furthermore, the use of just three conformational minima, sampling distinct regions of the ground state potential energy hypersurface, produces an adequate model of the experimentally observed low energy electronic transitions with significantly less computational effort than the finer-grained surveys used previously. In contrast to Figure 6, Figure S11 is calculated from six different conformers of [**2e**]$^{2+}$. However, these further three minima do not add any significant additional information and therefore do not change the appearance of the calculated spectrum.

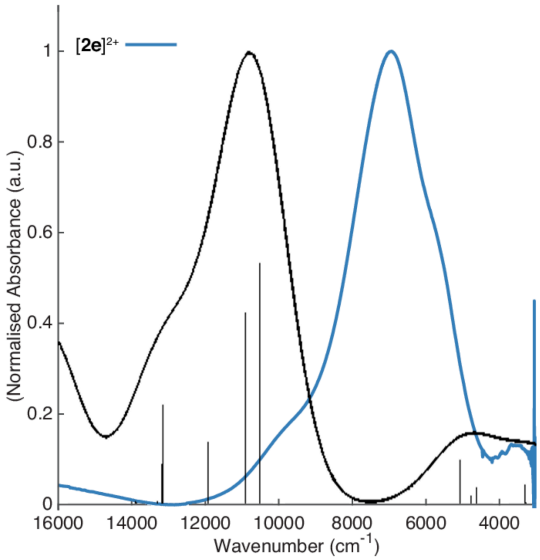

Figure 6. Overlay plot of the experimentally determined NIR spectra of [**2e**]$^{2+}$ (blue trace) with the normalised, line-broadened (900 cm^{-1}) stick spectrum from TDDFT calculations (lh-SsirPW92-D3/def2-SVP-COSMO(CH_2Cl_2)//BLYP35-D3/def2-SVP-COSMO(CH_2Cl_2)) from three representative minima ([**2e**]$^{2+}$ Ω = 70°, 82°, 180°) (black trace).

Electronic structures

The small number of conformational minima that provide an adequate description of the NIR spectra of [**1a – e**]$^{2+}$ and [**2a – e**]$^{2+}$ also provide a convenient basis from which to draw insight into the electronic structures of these compounds, which exist as an ensemble of conformations in fluid solution. As the electronic structure of each compound is sensitive to the conformation examined, the use of the multiple conformers in the computational analysis allows the character of the transitions responsible for those low energy electronic absorption band envelopes to be described more accurately than can be achieved by a single minimum energy structure (Table 3).

The homobimetallic ruthenium complex [**1a**]$^{2+}$ again serves as a convenient point to commence the discussion. At the lh-SsirPW92-D3/def2-SVP-COSMO(CH_2Cl_2)/BLYP35-D3/def2-SVP-COSMO(CH_2Cl_2) level of theory it is noted that for the *perp*-like lowest energy minimum (Ω = 68°), the SOMO is of π-symmetry, with nodal planes between the Ru-C, ≡C-C≡ and N-Ru atoms, and largely (47%) located on the N-coordinated ruthenium centre (Figure 7). Smaller contributions from the atoms of the C≡CC≡N bridging ligand (19%) and the C-coordinated metal (14%) are also noted. The HOMO and HOMO-2 have pronounced helical character, and are more concentrated on the carbon-coordinated metal and the bridge (Figure 7). The HOMO-1 is more metal in character and localised on the C-coordinated metal (Figure 7), whilst HOMO-3 has metal character from the N-coordinated metal. Turning attention to the other conformers of [**1a**]$^{2+}$, whilst the more *cis* (Ω = 40°) and *trans* (Ω = 138°) like structures offer similarly composed frontier orbitals to those described above for the *perp* (Ω = 68°) conformer, the degree of localisation is somewhat moderated (Figure 7). The spin-density distributions also show some minor variation with conformation (Figure 8), but overall the clear description of [**1a**]$^{2+}$ is of a localised Ru^{II}-C≡CC≡N-Ru^{III} mixed-valence system. In the case of [**1a**]$^{+}$ the Ru(C≡CC≡N)(dppe)Cp* moiety can therefore be considered as a strongly electron-donating metallo-ligand, which stabilises the oxidation of the N-coordinated {Ru(dppe)Cp*} fragment.

Table 3. Summary of selected computed ground-state structures (at the BLYP35-D3/def2-SVP-COSMO(CH_2Cl_2) level of theory), relative energies, S^2 expectation values and TDDFT excitation energies for conformational minima of compounds [**1a – e**]$^{2+}$ and [**2a – e**]$^{2+}$ at the lh-SsirPW92-D3/def2-SVP-COSMO(CH_2Cl_2)//BLYP35-D3/def2-SVP-COSMO(CH_2Cl_2) level of theory (see Tables S3 and S4 for results at other computational levels)

	Ω / °	<S^2>	ΔE / kJ mol^{-1}	E1 / cm^{-1}	E2 / cm^{-1}	E3 / cm^{-1}	E4 / cm^{-1}	E5 / cm^{-1}
[**1a**]$^{2+}$	40	0.76	12.1	3639	7529	7973	9548	12814
	49	0.76	3.8	3089	7072	7659	9737	12258
	68	0.76	0.0	3265	6846	7521	10201	12148
	138	0.76	17.7	3722	7552	7931	9418	12845
[**1b**]$^{2+}$	50	0.77	0.0	3486	5819	8838	10064	12168
	69	0.77	6.6	2037	4802	8786	9713	11612
	132	0.76	22.6	3293	6924	9377	10259	12627
[**1c**]$^{2+}$	4	0.76	0.0	4163	6076	8692	9060	11807
	78	0.76	25.1	3419	5334	8957	9839	11327
	158	0.77	11.9	3705	5683	8401	8490	11591
[**1d**]$^{2+}$	52	0.80	2.5	2063	5051	14144	14696	18272
	87	0.80	0.0	1901	4690	14027	15012	18044
	143	0.80	16.8	2169	5352	14143	14197	15499
[**1e**]$^{2+}$	51	0.78	0.0	3512	5270	11949	13976	16283
	85	0.78	3.5	3227	5146	12850	13409	16560
	134	0.78	15.1	3674	5407	12445	13443	16470
[**2a**]$^{2+}$	41	0.79	1.5	2298	4747	11325	13538	16715
	55	0.78	1.2	2243	4388	12202	13758	17115
	92	0.78	0.0	2110	4223	12040	13426	16678
[**2b**]$^{2+}$	71	0.79	0.0	2244	4306	12445	16096	17818
	81	0.78	2.4	2288	4197	12998	16576	18024
	179	0.79	24.7	2611	4802	12185	16238	18183
[**2c**]$^{2+}$	11	0.78	0.0	2681	4836	13319	15167	16923
	73	0.78	17.4	2626	4584	13668	15359	16936
	164	0.78	7.3	2399	4638	13136	13716	16431
[**2d**]$^{2+}$	46	0.80	2.7	1975	5007	12922	15435	18139
	94	0.80	0.0	1866	4723	14133	14164	15923
	130	0.80	9.0	1860	4943	13071	15494	18164
[**2e**]$^{2+}$	70	0.79	0.0	3302	5075	10908	13164	16335
	82	0.78	6.9	2931	4626	11914	13154	16367
	180	0.79	17.0	2552	4786	10519	13306	13881

10.1002/chem.201901200

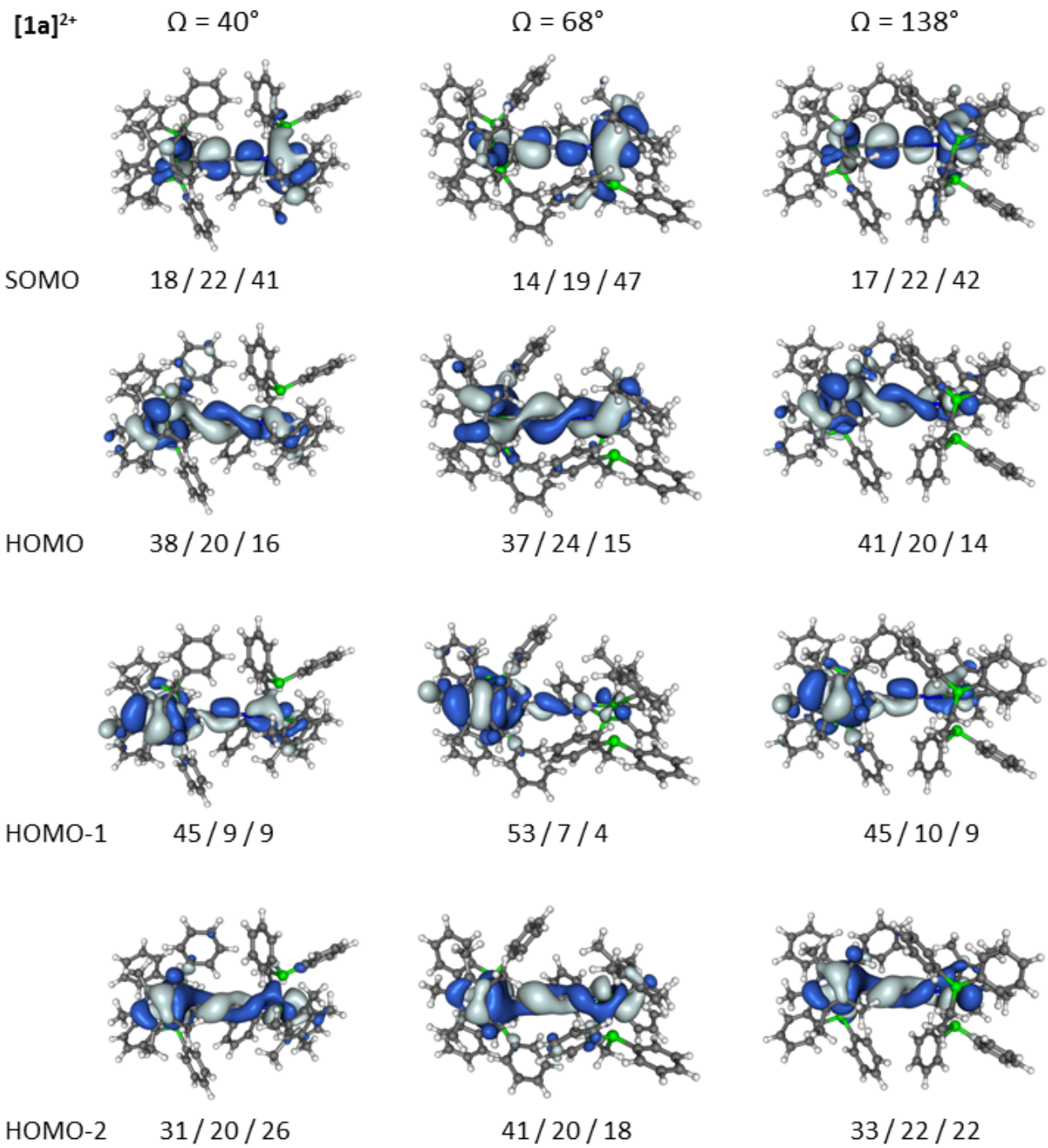

Figure 7. Plots of selected frontier molecular orbitals (isosurface: ±0.02 au) for conformers Ω = 40°, 68° and 138° of [**1a**]$^{2+}$. Compositions (%) of these orbitals are given Ru /C_3N / Ru at the lh-SsirPW92-D3/def2-SVP-COSMO(CH_2Cl_2)//BLYP35-D3/def2-SVP-COSMO(CH_2Cl_2) level. (See Tables S7a-d and S8a,b for MO compositions at other computational levels)

10.1002/chem.201901200

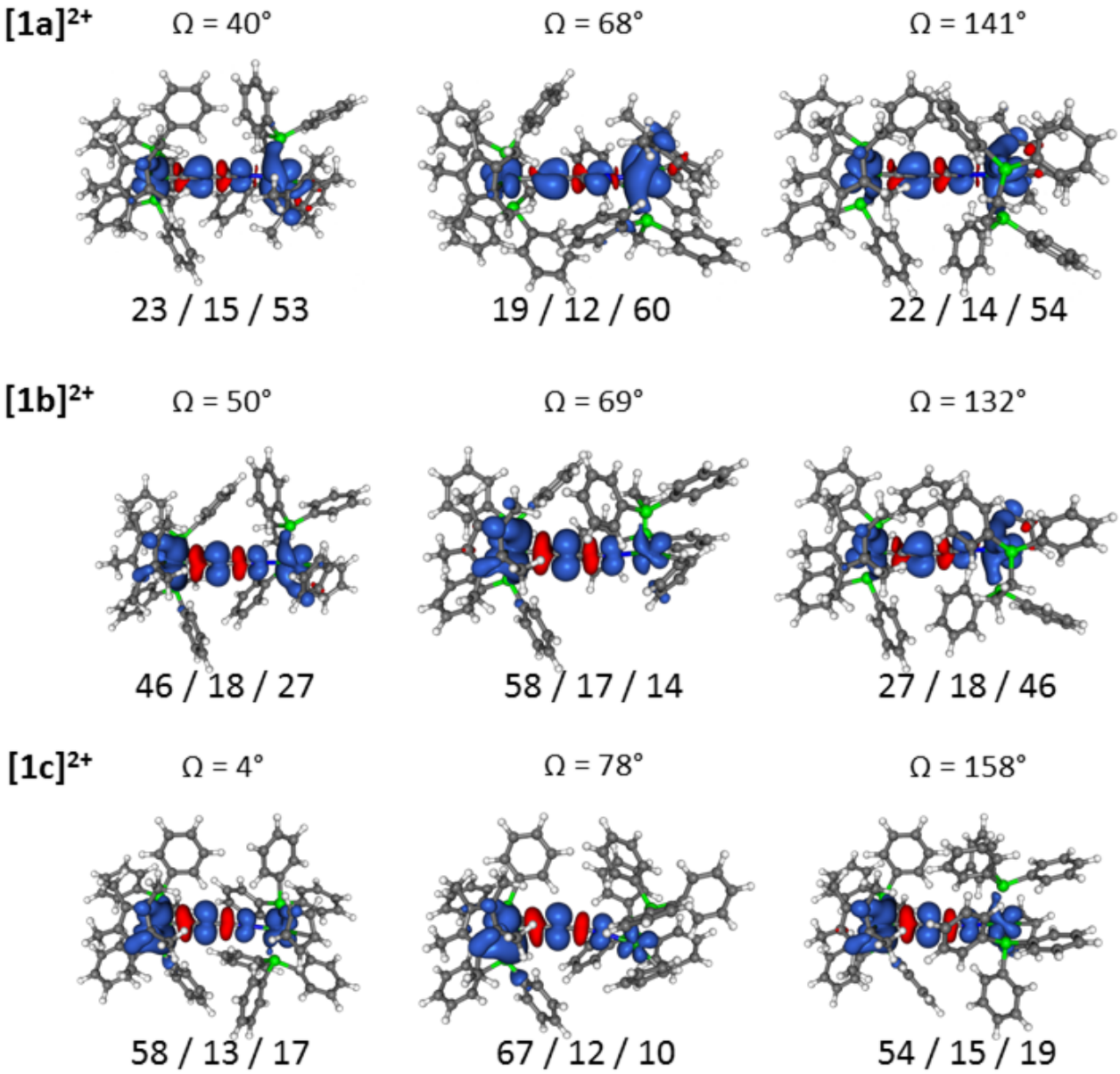

Figure 8. Plots of spin density (isosurface: ±0.001 au) for conformers of [**1a**]$^{2+}$, [**1b**]$^{2+}$, [**1c**]$^{2+}$. Relative atomic contributions are given M /C_3N / M' at the lh-SsirPW92-D3/def2-SVP-COSMO(CH_2Cl_2)//BLYP35-D3/def2-SVP-COSMO(CH_2Cl_2). (See Tables S5 and S6 for spin density compositions at other computational levels)

Importantly, the TDDFT results from the three sample minima of [**1a**]$^{2+}$ identify the lowest energy electronic transition (E_1) as falling not within the NIR band envelope, but rather in the IR region for each minimum structure (Ω = 40°, $\tilde{\nu}$ = 3639 cm^{-1}; Ω = 68°, $\tilde{\nu}$ = 3265 cm^{-1}; Ω = 138°, $\tilde{\nu}$ = 3722 cm^{-1}) (Table 3). These E_1 transitions have substantial HOMO-SOMO character

10.1002/chem.201901200

and are therefore well described as the lowest energy IVCT (i.e. Marcus-Hush style) transitions in a pseudo-octahedral d^6-d^5 mixed valence complex (Figure 9). Together, these transitions give rise to the low energy tail to the NIR band envelope which extends into the mid-IR (Figure 2), in a manner similar to that noted recently for [{Fe(dppe)Cp*}$_2$(μ-C≡CC≡C)]$^+$, which has been re-classified as valence-trapped on the IR time-scale,[7a] and also observed for related valence localised systems, such as [{Mo(dppe)(η-C$_7$H$_7$)}$_2$(μ-C≡CC≡C)]$^+$.[19]

The second and third excitations (E_2 and E_3) are calculated between 6846 – 7973 cm^{-1}, with varying degrees of (HOMO–1)-to-SOMO and (HOMO–3)-to-SOMO character. The lower energy maximum in the NIR band envelope (Figure 1) can therefore be attributed to the second IVCT transition expected from a d^6-d^5 mixed valence complex, overlapped with an interconfigurational (or dd) transition associated with the formally Ru^{III} centre (Figure 9).[3d] The E_4 excitations are calculated to fall between 9418 – 10201 cm^{-1}, arise from the (HOMO–2)-to-SOMO transitions, and therefore also have IVCT character as expected from the simple ligand field diagram of Figure 9. The weak intensity, highest energy shoulder on the NIR band envelope can be attributed to transitions from lower lying orbitals (HOMO–4 and HOMO–5) to the SOMO and can be described as the second interconfigurational (dd) transition.

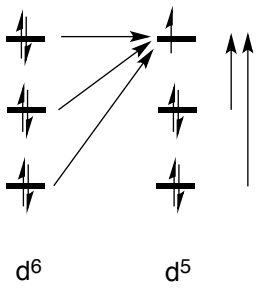

Figure 9. A schematic energy level diagram illustrating the three IVCT and two dd type electronic transitions in a pseudo-octahedral d^6/d^5 mixed valence complex.[3d]

With these general principles in hand, we briefly turn attention to the electronic structures of the other members of the series, which further illustrate the information that can be gleaned from consideration of the conformational population. For example, the {Ru(dppe)Cp} fragment is somewhat less electron-rich than the Ru(dppe)Cp* moiety, and [**1b**]$^{2+}$ presents a

10.1002/chem.201901200

scenario in which the site of oxidation is less clear than in [**1a**]$^{2+}$. Examination of [**1b**]$^{2+}$ reveals unexpected, but not unprecedented, variation in electronic structure with conformation (Figure 8, Figure 10).[8, 20] From the three minima chosen to sample the *cis*- (Ω = 50°), *perp*- (Ω = 69°) and *trans*- (Ω = 132°) regions of the conformational space, an initial examination of spin-density distribution (Figure 8) reveals the same trends towards the most localised structures associated with the most *perp*-like conformers as noted in [**1a**]$^{2+}$ and [{Ru(dppe)Cp*}$_2$(μ-C≡CC≡C)]$^+$. The lowest energy (E_1) transitions of these conformers of [**1b**]$^+$ are also found in the IR region and have IVCT (HOMO-SOMO) character (Table 3).

However, in contrast to [**1a**]$^+$, in the case of the *perp*-conformer of [**1b**]$^+$, oxidation takes places largely at the C-coordinated {Ru(dppe)Cp*} fragment, rather than at the N-coordinated Ru(dppe)Cp moiety, as indicated by both spin density distribution (Figure 8) and frontier orbital composition (Figure 10). In addition, whilst the *cis* (Ω = 50°) and *trans* (Ω = 132°) conformers give less polarised structures, the direction of the residual polarisation is reversed between these extremes. Thus the electron density along the Ru-C≡CC≡N-Ru chain is highly dependent on the relative orientation of the metal fragments as well as on the nature of the ancillary ligands. Therefore, whilst TDDFT calculations from each conformer confirm a similar pattern of electronic transitions with IVCT and interconfigurational / dd origin giving rise to the observed band-shapes of the low energy (NIR) band envelope, the character of the IVCT component (more localised vs more delocalised) and direction of electron transfer varies with conformation as the primary oxidation site (C- or N-coordinated metal fragment) shifts. The distribution of electronic characters in [**1b**]$^{2+}$ as function of conformation is also evident in the broadening of the ν(C≡CC≡N) vibrational bands in the mid-IR spectrum (Figure S12).

10.1002/chem.201901200

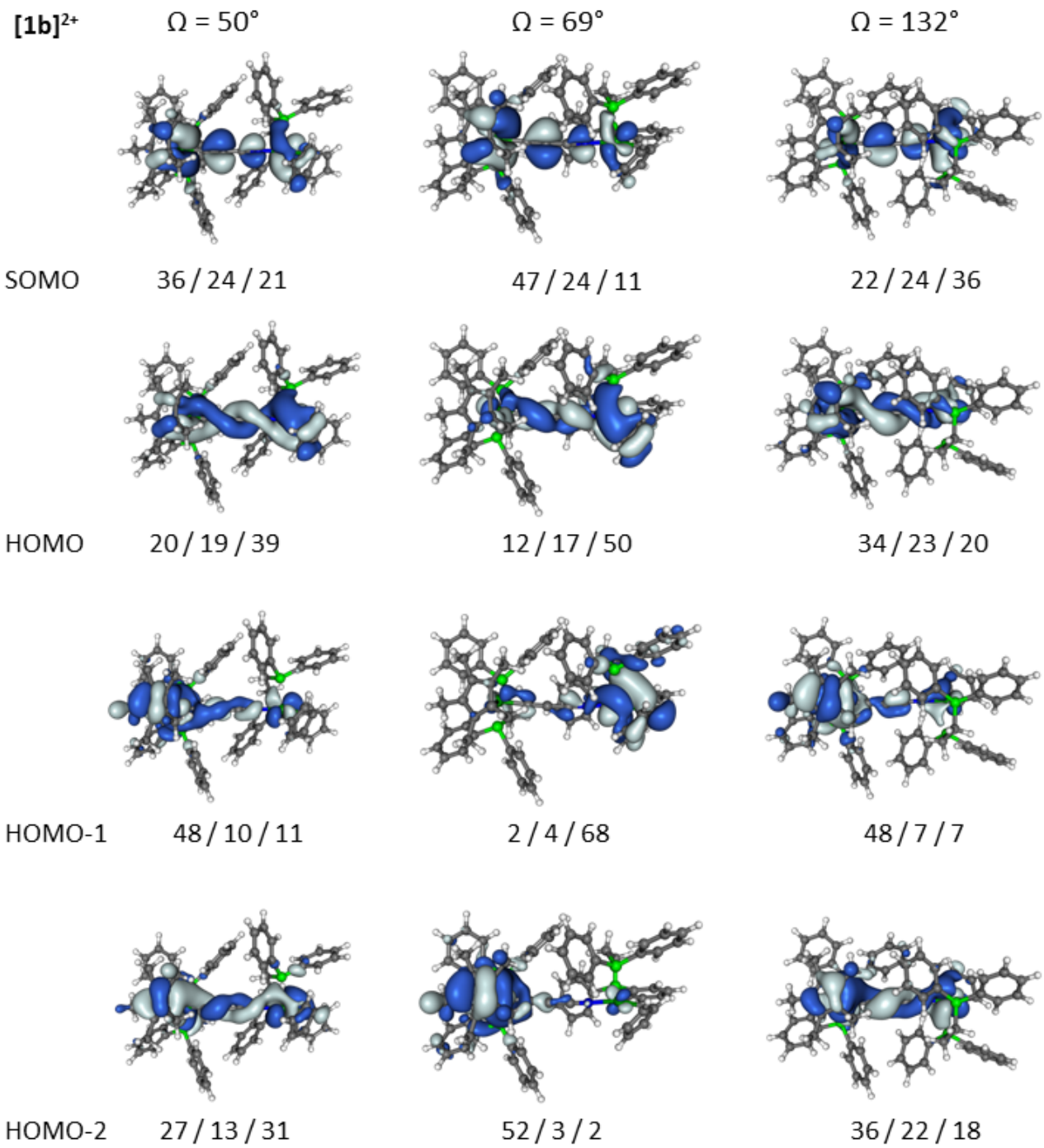

Figure 10. Plots of selected frontier molecular orbitals (isosurface: ±0.02 au) for conformers of [**1b**]$^{2+}$ (Ω = 50°, 69° and 132°). Compositions (%) of these orbitals are given Ru /C_3N / Ru at the lh-SsirPW92-D3/def2-SVP-COSMO(CH_2Cl_2)//BLYP35-D3/def2-SVP-COSMO(CH_2Cl_2). (See Tables S7a-d for MO compositions at other computational levels)

In contrast to the conformationally dependent redox isomers of [**1b**]$^{2+}$, the complex [{Cp*(dppe)Ru}(μ-C≡CC≡N){Ru(PPh$_3$)$_2$Cp}]$^{2+}$, [**1c**]$^{2+}$, with the less electron-rich Ru(PPh$_3$)$_2$Cp fragment coordinated at the N-end of the C≡CC≡N chain, gives rise to mixed-valence species in which the charge is consistently localised on the more electron-rich, C-coordinated Ru(dppe)Cp* fragment (Figure 8, Figure S13). For each of the structural minima used in the analysis (Ω = 4°, 78° and 158°), three of the four lowest energy electronic transitions (E_1, E_3, E_4) have appreciable IVCT character, whilst E_2 displays significant dd character (Table 3). This result is particularly useful, as the relatively low resolution of the experimental NIR band envelope observed for [**1c**]$^{2+}$ (Figure 4b) prevents any realistic attempt to properly resolve the overlapping transitions by conventional deconvolution methods, precluding the satisfactory application of a Marcus-Hush style analysis.

From examination of these initial examples it can be concluded that the features of the NIR spectra of the homo-bimetallic complexes [**1a** – **1c**]$^{2+}$ are adequately described by a small number of minima which sample the total conformational distribution. From analysis of the electronic structures of these minima, it can be observed that [**1a** – **1c**]$^{2+}$ offer more localised electronic structures than found for the structurally similar buta-1,3-diyn-1,4-diyl bridged complexes [{Ru(dppe)Cp*}$_2$(μ-C≡C-C≡C)]$^+$, [{Ru(dppe)Cp}$_2$(μ-C≡C-C≡C)]$^+$ and [{Ru(PPh$_3$)$_2$Cp}$_2$(μ-C≡C-C≡C)]$^+$. However, across both series the distribution of electron density is not only sensitive to the ancillary ligand set, but also influenced by the relative orientation of the half-sandwich end-caps. This leads to a further example of conformationally dependent redox-isomerism in the case of [**1b**]$^{2+}$. Thus, in every case, an analysis based on a single ground state minimum would fail to capture significant features of the electronic structures, which are in turn reflected in the appearance of the NIR band envelope.

The experimental NIR spectra of the heterobimetallic complexes [**1d**]$^{2+}$ and [**1e**]$^{2+}$, in which the electron-rich Fe(dppe)Cp* and Fe(dppe)Cp fragments are coordinated to the Ru(C≡CC≡N)(dppe)Cp* metallo-ligand, feature three distinct maxima at approximately 5000, 9000 and 12000 cm^{-1} ([**1d**]$^{2+}$, Figure 5), and 3500, 8000 and 11000 cm^{-1} ([**1e**]$^{2+}$, Figure S5). In the same manner as that described above, analyses of frontier orbital composition (Figure S14, Figure S15) and spin density distribution (Figure 11) indicate that the three minima chosen to sample the *cis*-, *perp*- and *trans*-regions of the ground state potential energy surfaces of [**1d**]$^{2+}$ (Ω = 52°, 87°, 143°) and [**1e**]$^{2+}$ (Ω = 51°, 85°, 134°) are well-described in

10.1002/chem.201901200

terms of a localised Ru^{II}-C≡CC≡CN-Fe^{III} electronic structure, with spin-density heavily localised on the iron atom in all conformations examined (Figure 11). In each complex [**1d**]$^{2+}$ and [**1e**]$^{2+}$, the Fe-centred dd transitions (E_1 and E_2) of the three sample conformers are calculated to fall in the region from the mid-IR to the low energy end of the NIR spectrum (Table 3). Thus, for these heterobimetallic radical dications, the low energy Fe^{III} dd bands fall in the same spectral range as the lowest energy IVCT bands of the weakly coupled homobimetallic ruthenium complexes [**1a – c**]$^{2+}$ (Table 3). Of the three IVCT bands associated with the pseudo-octahedral d^5-d^6 mixed valence complexes [**1d**]$^{2+}$ and [**1e**]$^{2+}$, the two lower energy bands fall in a narrow range of energies and give rise to the predominant apparent maximum near 9000 cm^{-1} in the experimental spectrum, whilst the third forms the higher energy shoulder at 12000 cm^{-1} (Figure S14, Figure S15, Table 3). The Ru^{II}-to-Fe^{III} charge transfer transitions (E3, E4 and E5) in [**1d**]$^{2+}$ and [**1e**]$^{2+}$ occur at higher energy than the Ru^{II}-to-Ru^{III} IVCT bands in [**1a – c**]$^{2+}$ (Table 3) consistent with the higher lying orbitals of the Fe(dppe)Cp* moiety.

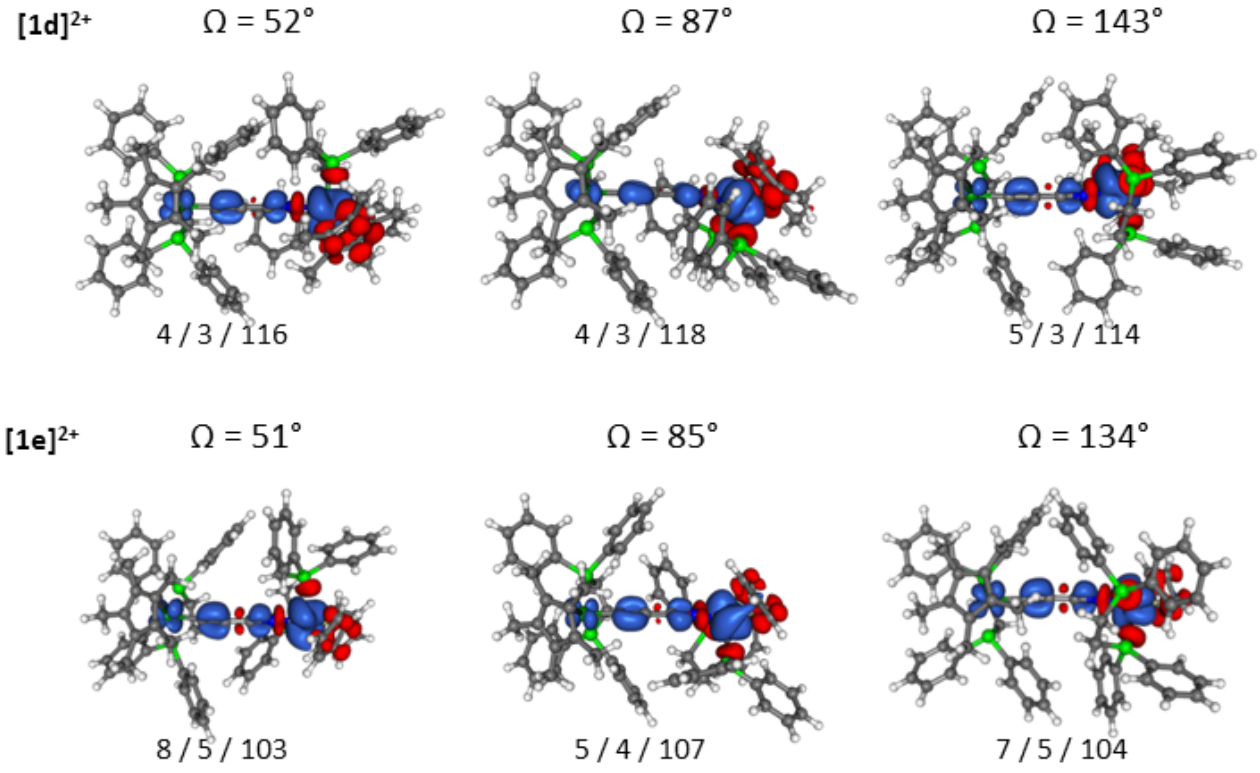

Figure 11. Plots of spin density (isosurface: ±0.001 au) for conformers [**1d**]$^{2+}$ and [**1e**]$^{2+}$. Relative atomic contributions are given Ru / C_3N / Fe at the lh-SsirPW92-D3/def2-SVP-COSMO(CH_2Cl_2)//BLYP35-D3/def2-SVP-COSMO(CH_2Cl_2) level of theory. Pronounced negative

10.1002/chem.201901200

spin-density envelopes at the oxidised iron moieties indicate substantial spin polarization, which may be connected to spin contamination in these systems (see text). (See Tables S5 and S6 for spin density compositions at other computational levels)

Similarly, on the basis of the calculated spin-density distributions (Figure 12), the hetero-bimetallic complexes [**2a - c**]$^{2+}$ are also well described in terms of a localised Fe^{III} and Ru^{II} electronic structure, but now with the Fe^{III} centre coordinated to the C-terminus of the C≡CC≡N ligand, in each conformation examined (Table 3). Low energy (NIR-IR) iron based dd transitions are observed, complemented by three higher energy IVCT bands. The highest energy IVCT transition shifts to higher energy as the ancillary ligands at Ru become less electron donating, thereby lowering the energy of the Ru-based donor.

10.1002/chem.201901200

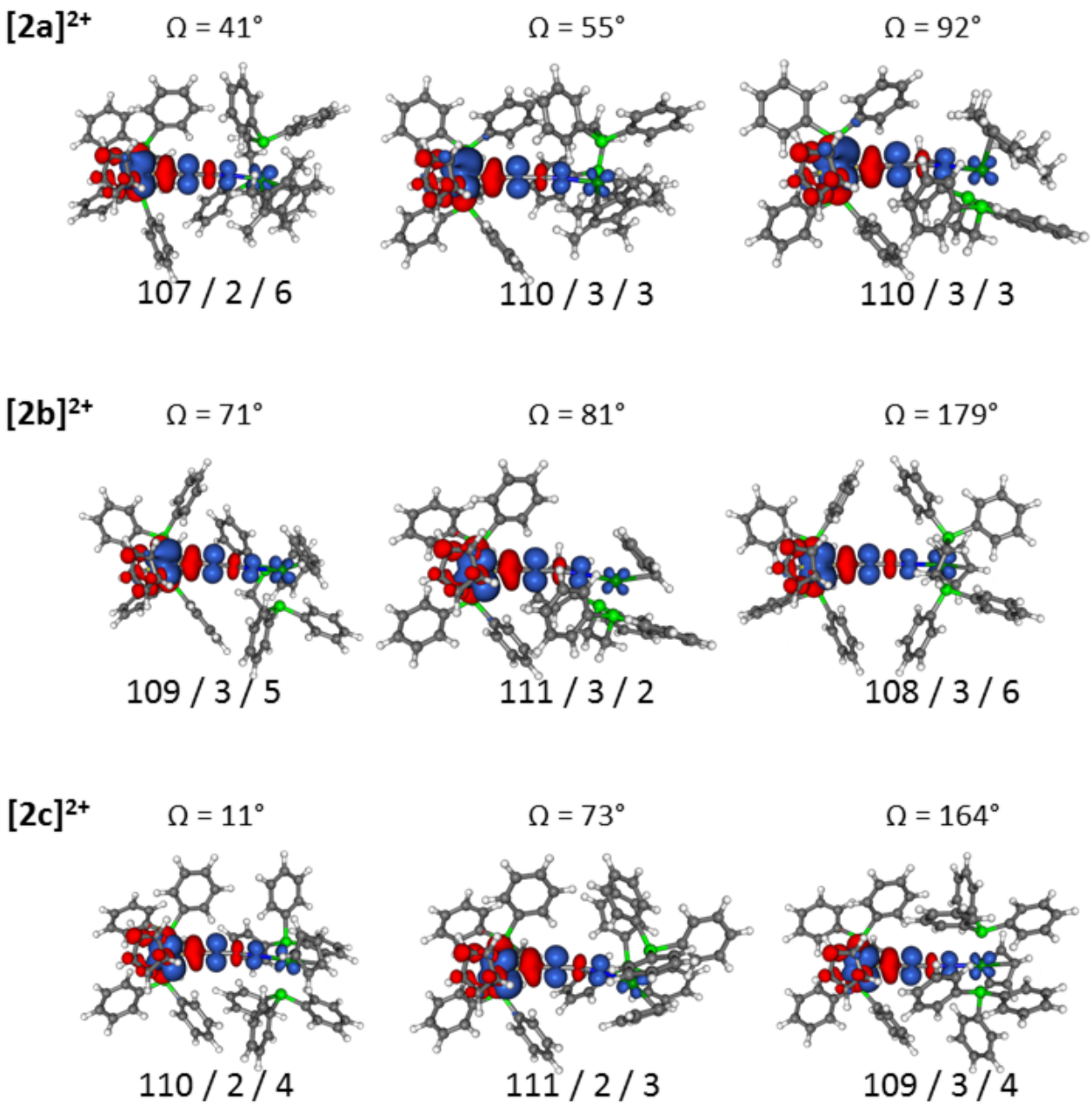

Figure 12. Plots of spin density (isosurface: ±0.001 au) for conformers [**2a**]$^{2+}$, [**2b**]$^{2+}$ and [**2c**]$^{2+}$. Relative atomic contributions are given Fe /C_3N / Ru at lh-SsirPW92-D3/def2-SVP-COSMO(CH_2Cl_2)//BLYP35-D3/def2-SVP-COSMO(CH_2Cl_2) level of theory. Pronounced negative spin-density envelopes at the oxidized iron moieties indicate substantial spin polarization, which may be connected to spin contamination in these systems (see text; see Figures S16-S18 and Tables S7b,c for MO compositions; see Table S5 for spin density compositions at other computational levels).

10.1002/chem.201901200

The homobimetallic iron complexes [{Cp(dppe)Fe}(μ-C≡CC≡N){Fe(dppe)Cp'}]$^{2+}$ (Cp' = Cp*, [**2d**]$^{2+}$; Cp' = Cp, [**2e**]$^{2+}$) behave similarly to the homo-bimetallic ruthenium complexes, with oxidation of [**2d**]$^{+}$ in all conformers examined taking place on the more electron-rich, N-coordinated Fe(dppe)Cp* fragment (Figure 13). These Fe^{II}-C≡CC≡CN-Fe^{III} compounds give rise to two low energy (NIR-IR) Fe^{III} dd bands (E1 and E2), consistent with earlier studies of 17-electron (Fe(III)) [FeX(dppe)Cp*]$^{+}$ complexes.[21] In the case of [**2d**]$^{2+}$, the transitions E3 and E4 with IVCT character are calculated between 11000 cm^{-1} and 13000 cm^{-1}, giving rise to the prominent absorption envelope observed experimentally in this region, whilst the third excitation occurs at much higher energy, computationally near 16300 cm^{-1}, in good agreement with the appearance of the experimental NIR band envelopes of these complexes (Figure S9). Complex [**2e**]$^{2+}$ behaves similarly (Figure 6), but also gives a further example of conformationally driven redox isomerism, with the *perp*-like conformers (Ω = 70, 82°) undergoing oxidation at the N-coordinated Fe(dppe)Cp metal site, whilst in the *trans*- (Ω = 180°) conformer the site of oxidation shifts to the C-coordinated metal fragment (Figure 13).

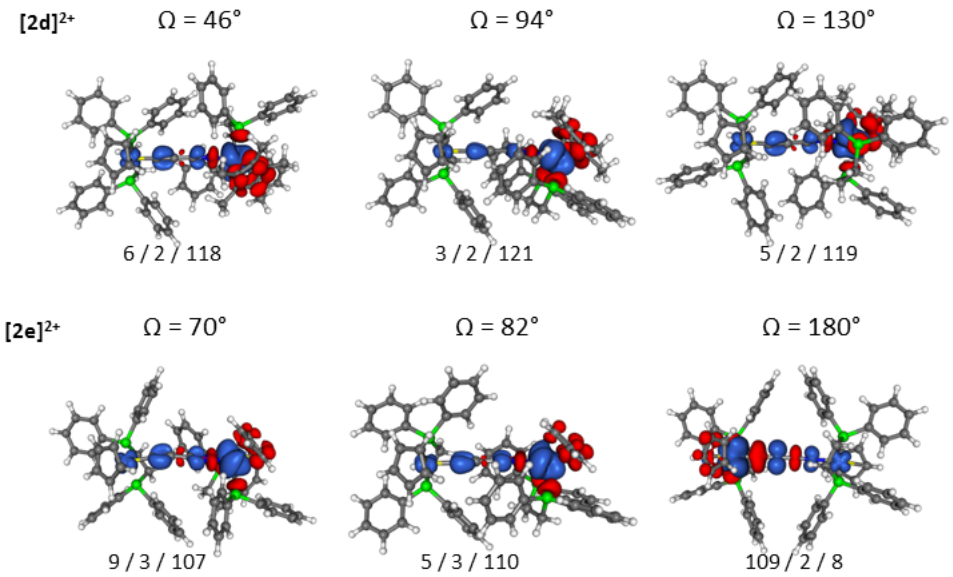

Figure 13. Plots of spin density (isosurface: ±0.001 au) for conformers [**2d**]$^{2+}$ and [**2e**]$^{2+}$. Relative atomic contributions are given Fe /C_3N / Fe at the lh-SsirPW92-D3/def2-SVP-COSMO(CH_2Cl_2)//BLYP35-D3/def2-SVP-COSMO(CH_2Cl_2). Pronounced negative spin-density envelopes at the oxidised iron moieties indicate substantial spin polarization, which may be connected to spin contamination in these systems (see text; see Figures S19, S20 and Tables

S7c,d, S8b for MO compositions; see Tables S5 and S6 for spin density compositions at other computational levels).

Conclusions

One-electron oxidation of the closed-shell bimetallic cyanacetylide-bridged cations [**1a – e**]$^{+}$ and [**2a – e**]$^{+}$ affords radical dications [**1a – e**]$^{2+}$ and [**2a – e**]$^{2+}$. As with other examples of conformationally mobile mixed-valence complexes, the NIR band envelopes of these species are not amenable to analysis using the relationships derived from Marcus-Hush owing to the presence of multiple, overlapping transitions of distinct electronic character. In these cases, an alternative analysis based on DFT calculations drawn from just three minima chosen to sample the major different regions of the ground state potential energy surface gives a good description of the low energy electronic transitions and hence the underlying electronic character of the relevant complex. The identification of further examples of conformationally driven redox-isomerism raises further reasons to be cautious in the application of Marcus-Hush analyses to complex NIR band-shapes. Here, dispersion-corrected structure optimizations of a small number of representative minima are used to model the experimentally relevant distribution of conformers. Using these few minima, TDDFT calculations (lh-SsirPW92-D3/def2-SVP-COSMO(CH_2Cl_2//BLYP35-D3/def2-SVP-COSMO(CH_2Cl_2)) gave excellent agreement with the experimentally observed spectral shapes, and far better than was achieved using the lowest energy minimum alone. We hope that this demonstration of a 'computationally minimal' approach to DFT analysis of conformationally diverse mixed-valence complexes will encourage other authors to explore similar approaches to further studies of not only mixed-valence systems, but also other examples of open-shell complexes and charge-transfer processes. Systematic blue shifts of the computed IVCT band maxima for the iron-localized complexes compared to the experimental spectra call for further refinement of the computational protocol (likely further improved exchange-correlation functionals are required) to minimise problems arising from spin contamination.

General Conditions

All reactions were carried out under an atmosphere of dry nitrogen using standard Schlenk techniques. Methanol and tetrahydrofuran were dried by passage over an alumina column and degassed before use, other solvents were standard reagent grade and used as received.

10.1002/chem.201901200

No special precautions were taken to exclude air or moisture during workup except where otherwise indicated. The compounds RuCl(dppe)Cp*,[15] [RuCl(dppe)Cp],[15] RuCl(PPh_3)$_2$-Cp,[22] FeCl(dppe)Cp*,[15] FeCl(dppe)Cp,[15] Ru(C≡CC≡N)(dppe)Cp*,[23] Fe(C≡CC≡CN)(dppe)Cp,[24] [**1a**]PF_6,[13b] [**1c**]PF_6[13b] and [**2c**]PF_6 [13a] were prepared according to previously published procedures. All other reagents were commercially available and used as received.

Cyclic voltammetry was carried out using a PalmSens Emstat^{3+} or Autolab PG-STAT 30 potentiostat, with platinum working, counter and pseudo-reference electrodes, from solutions in dichloromethane containing 0.1 M NBu_4PF_6 as the electrolyte, $\nu = 100$ mVs^{-1}. The decamethylferrocene/decamethylferrocinium couple was used as an internal reference for potential measurements such that Fc*H/Fc*H$^+$ falls at –0.48 V relative to external FcH/FcH$^+$ at 0.00 V.[17]

NMR spectra were recorded at 25 °C on Varian VNMRS 700 (^{1}H, 699.7 MHz; ^{13}C, 175.9 MHz), Varian VNMRS 600 (^{13}C, 150.8 MHz), Bruker Avance III 600 (^{1}H, 600.1 MHz; ^{31}P, 242.9 MHz), Bruker Avance III 500 (^{1}H, 500.1 MHz; ^{31}P, 202.4 MHz;) or Bruker Avance 400 (^{1}H, 400.1 MHz; ^{13}C, 100.6 MHz; ^{31}P, 161.9 MHz) spectrometers using $CDCl_3$ or CD_2Cl_2 as the solvent. Chemical shifts were determined relative to internal residual solvent signals (^{1}H, ^{13}C),[25] or external 85% H_3PO_4 (^{31}P $\delta = 0.0$ ppm). Spectroelectrochemistry was conducted in an OTTLE cell[26] using solutions in CH_2Cl_2 containing 0.1 M *n*Bu_4NPF_6 as the supporting electrolyte. Spectra were recorded on an Agilent Technologies Cary 660 FTIR, Agilent Technologies Cary 5000 UV-Vis-NIR or an Avantes diode array UV-Vis-NIR system comprising two light sources (UV-Vis: AvaLight-DH-S-Bal, Vis-NIR: AvaLight-Hal-S) and two spectrometers (UV-Vis: AvaSpec-ULS204-8L-USB2, NIR: AvaSpec-NIR256-2.5TEC) connected to a custom-built sample holder by bifurcated fibre optic cables. The Vis-NIR light source was attenuated with a band-pass filter transparent between ~900–4700 nm. Electrolysis in the cell was performed using a PalmSens Emstat^2 or Emstat^{3+} potentiostat at a scan rate of 10 mVs^{-1}.

FT-IR spectra were measured on an Agilent Technologies Cary 660 spectrometer or a Nicolet Avatar 360 spectrometer from solutions in dichloromethane in a thin layer cell fitted with CaF_2 windows or as Nujol mulls mounted between NaCl plates. EI-MS spectra were recorded on a Waters GCT Premier mass spectrometer coupled with an Agilent GC 7890A GC, ESI-MS

were recorded on a Waters LCT Premier XE mass spectrometer in positive mode from solutions in acetonitrile. Elemental analyses were performed at the London Metropolitan University.

Details of the crystallographic procedures are given in the SI, and crystallographic data for the structure have been deposited with the Cambridge Crystallographic Data (CCDC-1901974-1901980)

[{Cp(dppe)Ru]}(μ-C≡CC≡N){Ru(dppe)Cp}]PF_6 ([**1b**]PF_6)*

A mixture of Ru(C≡CC≡N)(dppe)Cp* (54.0 mg, 78.9 μmol), RuCl(dppe)Cp (47.0 mg, 78.9 μmol) and NH_4PF_6 (52.0 mg, 315 μmol) and methanol (3 ml) was heated to reflux for 105 min and then left to cool slowly to room temperature whereupon a yellow precipitate was visible in a yellow solution. This bright yellow precipitate was collected by filtration, washed with cold methanol (10 ml) and hexanes (2 × 20 ml) and dried in air affording the product as a bright yellow powder (84.3 mg, 77%), which was recrystallised (slow diffusion, $CHCl_3$/hexane) to give the $0.5CHCl_3$ solvate. IR (CH_2Cl_2, cm^{-1}): 1985s ν(C≡C), 2198s ν(C≡N). ^1H NMR (699.7 MHz, $CDCl_3$) δ / ppm: 1.31 (s, 15H, $C_5(CH_3)_5$), 1.87 – 1.99 (m, 2H, CH_2), 2.03 – 2.13 (m, 2H, CH_2), 2.13 – 2.23 (m, 2H, CH_2), 2.47 – 2.39 (m, 2H, CH_2), 4.50 (s, 5H, C_5H_5), 6.97 – 7.56 (m, 40H, C_6H_5). ^{13}C NMR (175.9 MHz, $CDCl_3$) δ / ppm: 9.8 (s, $C_5(CH_3)_5$), 27.5 (t, J_{C-P} = 24 Hz, CH_2), 29.0 (t, J_{C-P} = 24 Hz, CH_2), 78.0 (s, C_β), 81.2 (s, C_5H_5), 94.5 (s, $C_5(CH_3)_5$), 114.2 (s, C_γ), 127.5 – 136.1 (m, C_6H_5), 138.0 (t, J_{C-P} = 22 Hz, C_α). ^{31}P NMR (161.9 MHz, $CDCl_3$) δ / ppm: 77.4 (s, dppe), 78.7 (s, dppe). MALDI (+)-MS : *m/z* 1250 $[M - PF_6]^+$. Found: C, 60.20; H, 4.79; N, 0.98. Calc. for $C_{70}H_{68}F_6NP_5Ru_2$: C, 60.30; H, 4.92; N, 1.00 %. This complex visibly discolours quickly after isolation, even under inert atmosphere, eventually forming a grey powder.

[{Cp(dppe)Ru}(μ-C≡CC≡N){Fe(dppe)Cp*}]PF_6 ([**1d**]PF_6)*

A mixture of Ru(C≡CC≡N)(dppe)Cp* (100 mg, 146 μmol), [FeCl(dppe)Cp*]•CH_2Cl_2 (105 mg, 146 μmol), NH_4PF_6 (26.0 mg, 161 μmol) and methanol (5 mL) was heated to reflux for 1.5 h and then allowed to cool to ambient temperature. Subsequently the solvent was removed under reduced pressure and the residue was dissolved in dichloromethane (3 mL) and filtered into rapidly stirring hexanes (60 mL) affording the product as a deep pink powder which was recovered by filtration, washed with hexanes (2 × 10 mL) and dried in air.

(191 mg, 92%). Recrystallisation (slow diffusion, CH_2Cl_2/hexane) afforded single crystals as the $2.5CH_2Cl_2$ solvate. IR (CH_2Cl_2, cm^{-1}): 1979 ν(C≡C), 2182 ν(C≡N). ^1H NMR (500.1 MHz, $CDCl_3$) δ / ppm: 1.11 (vbr, 15H, $FeC_5(CH_3)_5$), 1.52 (s, 15H, $RuC_5(CH_3)_5$), 1.81–2.04 (m, 4H, CH_2), 2.16 (m, 2H, CH_2), 2.38 (m, 2H, CH_2), 7.10 (m, 4H, C_6H_5) 7.18–7.53 (m, 36H, C_6H_5). ^{31}P NMR (202.4 MHz, $CDCl_3$) δ / ppm: 78.8 (br s, dppe), 90.0 (br s, dppe). The ^{13}C NMR spectrum was substantially broadened in $CDCl_3$ as is common in our experience for Fe(dppe)Cp* complexes[15] and not informative. Found: C, 60.85; H, 5.25; N, 0.98. Calc. for $C_{75}H_{78}F_6FeNP_5Ru•CH_2Cl_2$: C, 60.45; H, 5.28; N, 0.94 %.

[{Cp(dppe)Ru}(μ-C≡CC≡N){Fe(dppe)Cp}]PF_6 ([**1e**]PF_6)*

A mixture of Ru{C≡CC≡N}(dppe)Cp* (0.081 g, 118 μmol), FeCl(dppe)Cp (66.0 g, 118 μmol), NH_4PF_6 (21.0 mg, 130 μmol) was stirred for twenty minutes before being refluxed for 2 h. Over this time, the solution colour changed from orange to deep red. The solution was filtered, the filtrate concentrated to dryness and the dark red residue was dissolved in dichloromethane and filtered into rapidly stirring hexanes (60 mL) affording the product as a red powder which was recovered by filtration, washed with hexanes (3 × 20 mL) and dried in air (130 mg, 81%). Recrystallisation (slow diffusion, CH_2Cl_2/hexane) afforded crystals of the CH_2Cl_2 solvate suitable for X-ray analysis. IR (CH_2Cl_2, cm^{-1}): 1978 ν(C≡C), 2186 ν(C≡N). ^1H NMR (400.0 MHz, $CDCl_3$) δ / ppm: 1.41 (s, 15H, $C_5(CH_3)_5$), 1.95 – 2.11 (m, 4H, -CH_2, dppe), 2.13 – 2.23 (m, 2H, CH_2), 2.38 – 2.49 (m, 2H, CH_2), 4.19 (s, 5H, C_5H_5), 7.06 – 7.68 (m, 40H, C_6H_5). ^{13}C NMR (175.9 MHz, $CDCl_3$) δ / ppm: 9.8 (s, $C_5(CH_3)_5$), 26.8 – 27.6 (m, CH_2), 28.7 – 29.1 (m, CH_2), 78.6 (s, C_5H_5), 94.6 (s, $C_5(CH_3)_5$), 121.6 (s, C_γ), 127.5- 133.1 (m, C_6H_5), 135.8 (t, J_{C-P} = 27 Hz, C_α). ^{31}P NMR (161.9 MHz, $CDCl_3$) δ / ppm: 77.6 (s, dppe), 96.7 (s, dppe). MALDI (+)-MS (*m*/*z*): 1204 $[M - PF_6]^+$. Found: C, 62.28; H, 4.96; N, 1.08. Calc. for $C_{70}H_{68}F_6FeNP_5Ru$: C, 62.32; H, 5.08; N, 1.04 %.

[{Cp(dppe)Fe}(μ-C≡CC≡N){Ru(dppe)Cp}]PF_6 ([**2a**]PF_6)*

A mixture of Fe{C≡CC≡N}(dppe)Cp (70.0 mg, 123 μmol), RuCl(dppe)Cp* (74.0 mg, 111 μmol), NH_4PF_6 (72.0 mg, 441 μmol), methanol (15 ml) and tetrahydrofuran (10 ml) was heated to reflux for 2 h and then left to cool slowly to ambient temperature. The solution colour darkened from orange to brown over the reflux period. Subsequently the solvent was removed under reduced pressure and the residue was dissolved in dichloromethane and filtered into rapidly stirring hexanes affording the product as a yellow powder which was

recovered by filtration, washed with hexanes (3 × 20 mL) and dried in air (140 mg, 94%) before being recrystallised (slow cooling of a hot MeOH solution) to give single crystals suitable for X-ray diffraction. IR (nujol, cm^{-1}): 1979 ν(C≡C), 2189 ν(C≡N). ^{1}H NMR (400.1 MHz, $CDCl_3$) δ / ppm: 1.25 (s, 15H, $C_5(CH_3)_5$), 1.94 – 2.01 (m, 2H, CH_2), 2.01 – 2.08 (m, 2H, CH_2), 2.10 – 2.29 (m, 4H, CH_2), 4.19 (s, 5H, C_5H_5), 7.02 – 7.50 (m, 40H, C_6H_5). ^{13}C NMR (100.6 MHz, $CDCl_3$) δ / ppm: 9.5 (s, $C_5(CH_3)_5$), 27.6 – 28.2 (m, CH_2), 81.3 (s, C_5H_5), 91.9 (s, $C_5(CH_3)_5$), 127.8 – 133.1 (m, C_6H_5). ^{31}P NMR (161.9 MHz, $CDCl_3$) δ / ppm: 73.6 (s, dppe), 101.6 (s, dppe). MALDI (+)-MS (*m*/*z*): 1204 [{Cp(dppe)Fe}-C≡CC≡N-{Ru(dppe)Cp*}]$^+$; 635 [Ru(dppe)Cp*]$^+$. Found: C, 62.41; H, 4.96; N, 1.04. Calc. for $C_{70}H_{68}F_6FeNP_5Ru$: C, 62.32; H, 5.08; N, 1.04 %.

*[{Cp(dppe)Fe}(μ-C≡CC≡N){Ru(dppe)Cp}]PF_6 ([**2b**]PF_6)*

A mixture of Fe{C≡CC≡N}(dppe)Cp (72.0 mg, 126 μmol), RuCl(dppe)Cp (84.0 mg, 139 μmol), NH_4PF_6 (89.0 mg, 548 μmol), methanol (15 ml) and tetrahydrofuran (10 ml) was heated to reflux for 4 h and then allowed to cool to ambient temperature. Subsequently the solvent was removed from the bright orange solution under reduced pressure. The resulting residue was dissolved in dichloromethane and filtered into rapidly stirring hexanes affording the product as a yellow powder which was recovered by filtration, washed with hexanes (3 × 20 mL) and dried in air (110 mg, 68%). Recrystallisation of the sample (slow diffusion, CH_2Cl_2/pentane) gave crystals suitable for single-crystal X-ray diffraction. IR (nujol, cm^{-1}): 1979 ν(C≡C), 2192 ν(C≡N). ^{1}H NMR (400.0 MHz, $CDCl_3$) δ / ppm: 2.05 – 2.24 (m, 6H, CH_2), 2.24 – 2.46 (m, 2H, CH_2), 4.20 (s, 5H, C_5H_5), 4.52 (s, 5H, C_5H_5), 7.01 – 7.80 (m, 40H, C_6H_5). ^{13}C NMR (150.8 MHz, $CDCl_3$) δ / ppm: 27.5 (t, J_{C-P} = 21 Hz, CH_2), 28.0 (t, J_{C-P} = 24 Hz, CH_2), 80.9 (s, C_β), 81.0 (s, C_5H_5), 81.2 (s, C_5H_5), 108.8 (s, C_γ) 127.8 – 133.2 (m, C_6H_5), 138.0 (t, J_{C-P} = 25 Hz, C_α). ^{31}P NMR (161.9 MHz, $CDCl_3$) δ / ppm: 78.3 (s, dppe), 101.3 (s, dppe). MALDI (+)-MS (*m*/*z*): 1134 [M – PF_6]$^+$; 570 [Fe{C≡CC≡N}(dppe)Cp]$^+$. Found: C, 60.95; H, 4.44; N, 1.16. Calc. for $C_{65}H_{68}F_6FeNP_5Ru$: C, 61.04; H, 4.57; N, 1.10 %.

[{Cp(dppe)Fe}(μ-C≡CC≡N){Fe(dppe)Cp}]PF_6 ([**2d**]PF_6)*

A mixture of Fe{C≡CC≡N}(dppe)Cp (70.0 mg, 123 μmol), [FeCl(dppe)Cp*]•CH_2Cl_2 (88.0 mg, 123 μmol), NH_4PF_6 (22.0 mg, 135 μmol) and methanol (5 mL) was heated to reflux for 2.5 h and then allowed to cool to ambient temperature. Subsequently the solvent was removed under reduced pressure and the residue was dissolved in dichloromethane (3 mL) and

filtered into rapidly stirring hexanes (150 mL) affording the product as a peach powder which was recovered by filtration, washed with hexanes (20 mL) and dried in air (137 mg, 86%) before being recrystallised (slow cooling of a hot MeOH solution) to give single crystals suitable for X-ray diffraction. IR (CH_2Cl_2, cm^{-1}): 1977 ν(C≡C), 2180 ν(C≡N). ^{1}H NMR (600.1 MHz, CD_2Cl_2) δ / ppm: 1.14 (vbr, 15H, $FeC_5(CH_3)_5$), 1.80 (vbr, 4H, CH_2), 2.28 (br m, 4H, CH_2), 4.35 (s, 5H, FeC_5H_5), 7.15 (m, 4H, C_6H_5) 7.25–7.54 (m, 32H, C_6H_5), 7.61 (m, 4H, C_6H_5). ^{31}P NMR (242.9 MHz, CD_2Cl_2) δ / ppm: 90.2 (br s, dppe), 102.5 (br s, dppe). The ^{13}C NMR spectrum was substantially broadened in $CDCl_3$ as is common in our experience for Fe(dppe)Cp* complexes[15] and not informative. Found: C, 64.61; H, 5.22; N, 1.08. Calc. for $C_{70}H_{68}F_6Fe_2NP_5$: C, 64.48; H, 5.26; N, 1.07 %.

*[{Cp(dppe)Fe}(μ-C≡CC≡N){Fe(dppe)Cp}]PF_6 ([**2e**]PF_6)*

A mixture of Fe{C≡CC≡N}(dppe)Cp (59.0 mg, 103 μmol), FeCl(dppe)Cp (57.0 mg, 103 μmol), NH_4PF_6 (67.0 mg, 413 μmol) and methanol (10 ml) was heated to reflux for 1 h, changing colour from a black to a deep red solution. Subsequently the reaction mixture was allowed to cool to ambient temperature and the solvent was removed under reduced pressure. The resulting residue was dissolved in dichloromethane and filtered into rapidly stirring hexanes affording the product as a red powder which was recovered by filtration, washed with hexanes (3 × 10 ml) and dried in air (75.0 mg, 58%) before being recrystallised (slow diffusion, CH_2Cl_2/hexane) to give single crystals of the bis(CH_2Cl_2) solvate suitable for X-ray diffraction. IR (CH_2Cl_2, cm^{-1}): 1975 ν(C≡C), 2185 ν(C≡N). ^{1}H NMR (699.7 MHz, $CDCl_3$) δ / ppm: 1.87 – 1.95 (m, 2H, CH_2), 2.09 – 2.16 (m, 2H, CH_2), 2.22 – 2.33 (m, 4H, CH_2), 4.10 (s, 5H, C_5H_5), 4.19 (s, 5H, C_5H_5), 7.05 – 7.70 (m, 40H, C_6H_5). ^{13}C NMR (175.9 MHz, $CDCl_3$) δ / ppm: 27.3 (t, J_{C-P} = 22 Hz, CH_2), 28.0 (t, J_{C-P} = 22 Hz, CH_2), 78.5 (s, C_5H_5), 81.3 (s, C_5H_5), 88.6 (s, C_β), 119.8 (s, C_γ), 127.9 – 139.5 (m, C_6H_5), 137.8 (t, J_{C-P} = 22 Hz, C_α). ^{31}P NMR (161.9 MHz, $CDCl_3$) δ / ppm: 96.2 (s, dppe), 101.6 (s, dppe). MALDI (+)-MS (*m*/*z*): 1088 [M – PF_6]$^+$. Found: C, 63.21; H, 4.75; N, 1.20. Calc. for $C_{65}H_{58}F_6Fe_2NP_5$: C, 63.28; H, 4.74; N, 1.14 %.

Computational Details

The structures being presented here were optimised and the analyses of their properties were performed using versions of the TURBOMOLE software package[27], locally modified by the Berlin group. Unless noted otherwise, the global hybrid functional BLYP35[10d] was used for all structure optimizations (and vibrational frequency calculations). The BLYP35 function

is based on the B88 exchange and LYP correlation functional[28] using 35% Hartree-Fock admixture, and which has proven to be effective in describing the electronic character of localised and delocalised, organic[10c, 10d] and organometallic mixed-valence complexes.[8c] [8a, 8b, 29] The COSMO continuum solvent model was used for dichloromethane (CH_2Cl_2, ε = 8.93) in all calculations[30] Calculations of vibrational frequencies were performed by numerical differentiation of analytical gradients using TURBOMOLE's NumForce script (SCF convergence 10^{-8} E_h), with the absence of imaginary frequencies indicating the identification of true minima. In view of systematically blue-shifted IVCT band maxima, we also examined structures obtained with the B3LYP functional as a basis for TDDFT computations of excitation spectra using different functionals.

As was found in earlier studies with butadiyndiyl-bridged iron complexes reported elsewhere,[7a] spin contamination and poor reproduction of the excitation energies using BLYP35 was observed in the iron-containing complexes of the current study ([**1d,e**]$^{2+}$,[**2a-e**]$^{2+}$). Following the protocol developed in the previous study, structures from BLYP35 optimisations were used to do single-point energy and linear-response TDDFT excitation-energy calculations with the local hybrid functional Lh-SsirPW92 having position-dependent Hartree-Fock admixture and a partially self-interaction-corrected correlation part.[12] The local hybrid functional is constructed according to

$$E_{\mathrm{X}}^{Lh} = \int a(\mathbf{r})\,\varepsilon_{\mathrm{X}}^{\mathrm{exact}}(\mathbf{r})\mathrm{d}\mathbf{r} + \int\left[1 - a(\mathbf{r})\right]\varepsilon_{\mathrm{X}}^{\mathrm{DFT}}(\mathbf{r})\mathrm{d}\mathbf{r} + E_{\mathrm{C}}^{\mathrm{DFT}}$$

where the real-space dependent local mixing function $a(\mathbf{r})$ replaces the constant admixture parameter a (global hybrid functional, e.g. 0.35 for BLYP35, 0.20 for B3LYP), with

$a(\mathbf{r}) = 0.646\,\tau_W/\tau$,

where τ_W and τ are the von Weizsäcker and the Kohn-Sham kinetic-energy densities, respectively.

Since the TDDFT results from BLYP35 optimised structures of butadiyndiyl-bridged bis(ruthenium) complexes were found to be essentially the same with both BLYP35 and the Lh-SsirPW92 calculations,[7a] this protocol (Lh-SsirPW92 TDDFT calculations on structures from BLYP35 optimisation) was applied on all compounds in the present study.

The def2-SVP basis sets were used for all calculations.[31] Earlier calculations on butadiyndiyl-bridged ruthenium complexes using larger basis sets (def2-TZVP) gave negligible changes in structure and spectroscopic parameters.[8a] Furthermore, a grid size of m5 (grid 3 for the SCF iterations, grid 5 for the final energy evaluation) was applied. All computations added Grimme's DFT-D3 atom-additive semi-empirical dispersion correction terms, both for structure optimisations and vibrational frequency analyses, as well as energy computations.[32] The DFT-D3 parameters used here are $rs_6 = 1.1225$ and $s_8 = 0.9258$ optimized for the BLYP35 functional[11a] and $rs_6 = 0.77$ and $s_8 = 1.429$ for the Lh-SsirPW92 functional.[33] For sake of completeness, the DFT-D3 parameters for B3LYP are rs6 = 1.261 and s8 = 1.703, respectively.[32]

Acknowledgments.

We gratefully acknowledge funding from the ARC (DP 140100855, FT 120100073) and DFG (KA1187/13-2). This work was further supported through activities undertaken with the support of a Friedrich Wilhelm Bessel Research Award to PJL from the Alexander-von-Humboldt foundation. This project has been greatly enhanced by funding from the DAAD/Go8 enabling exchange visits of PJL, JBGG, SG and MK between Perth and Berlin. Further support from the Berlin excellence cluster "Unifying systems in catalysis" of Deutsche Forschungsgemeinschaft (DFG, German Research Foundation) under Germany´s Excellence Strategy – EXC 2008/1 (UniSysCat) – 390540038" is gratefully acknowledged. This project was further supported by the North-German Supercomputing Alliance (HLRN), which provided HPC resources.

References

[1] (a) B. S. Brunschwig, N. Sutin, *Coord. Chem. Rev.* **1999**, *187*, 233-254; (b) A. Palii, B. Tsukerblat, J. M. Clemente-Juan, S. M. Aldoshin, *J. Phys. Chem. A* **2015**, *119*, 9844-9856;

(c) S. F. Nelsen, K. P. Schultz, J. P. Telo, *J. Phys. Chem. A* **2008**, *112*, 12622-12628; (d) S. F. Nelsen, M. N. Weaver, Y. Luo, J. V. Lockard, J. I. Zink, *Chem. Phys.* **2006**, *324*, 195-201; (e) A. Lami, *Chem. Phys.* **2001**, *273*, 159-167; (f) S. B. Piepho, *Mixed Valency Systems : Applications in Chemistry, Physics and Biology* **1991**, *343*, 329-334; (g) C. Creutz, *Prog. Inorg. Chem.* **1983**, *30*, 1-73.

[2] A. Heckmann, C. Lambert, *Angew. Chem. Int. Ed.* **2012**, *51*, 326-392.

[3] (a) F. Paul, C. Lapinte, *Coord. Chem. Rev.* **1998**, *178*, 431-509; (b) W. Kaim, A. Klein, M. Glöckle, *Acc. Chem. Res.* **2000**, *33*, 755-763; (c) A. Ceccon, S. Santi, L. Orian, A. Bisello, *Coord. Chem. Rev.* **2004**, *248*, 683-724; (d) K. D. Demadis, C. M. Hartshorn, T. J. Meyer, *Chem. Rev.* **2001**, *101*, 2655-2685.

[4] B. S. Brunschwig, C. Creutz, N. Sutin, *Chem. Soc. Rev.* **2002**, *31*, 168-184.

[5] M. B. Robin, P. Day, *Adv. Inorg. Chem. Radiochem.* **1967**, *10*, 247 - 422.

[6] (a) C. Hassenrück, A. Mang, R. F. Winter, *Inorg Chem* **2019**, *58*, 2695-2707; (b) C. Hassenruck, R. F. Winter, *Inorg Chem* **2017**, *56*, 13517-13529; (c) C. Hassenrück, P. Mucke, J. Scheck, S. Demeshko, R. F. Winter, *Eur. J. Inorg. Chem.* **2017**, 401-411.

[7] (a) S. Gückel, J. B. G. Gluyas, S. El-Tarhuni, A. N. Sobolev, M. W. Whiteley, J.-F. Halet, C. Lapinte, M. Kaupp, P. J. Low, *Organometallics* **2018**, *37*, 1432-1445; (b) D. M. D'Alessandro, F. R. Keene, *Chem. Soc. Rev.* **2006**, *35*, 424-440; (c) W. Kaim, B. Sarkar, G. K. Lahiri, in *Spectroelectrochemistry* (Eds.: W. Kaim, A. Klein), Royal Society of Chemistry, Cambridge, UK, **2008**.

[8] (a) J. B. G. Gluyas, S. Gückel, M. Kaupp, P. J. Low, *Chem. Eur. J.* **2016**, *22*, 16138-16146; (b) M. Parthey, J. B. G. Gluyas, M. A. Fox, P. J. Low, M. Kaupp, *Chem. Eur. J.* **2014**, *20*, 6895-6908; (c) M. Parthey, J. B. G. Gluyas, P. A. Schauer, D. S. Yufit, J. A. K. Howard, M. Kaupp, P. J. Low, *Chem. Eur. J.* **2013**, *19*, 9780-9784.

[9] (a) M. I. Bruce, B. G. Ellis, P. J. Low, B. W. Skelton, A. H. White, *Organometallics* **2003**, *22*, 3184-3198; (b) M. I. Bruce, P. J. Low, K. Costuas, J. F. Halet, S. P. Best, G. A. Heath, *J. Am. Chem. Soc.* **2000**, *122*, 1949-1962.

[10] (a) M. Renz, M. Kess, M. Diedenhofen, A. Klamt, M. Kaupp, *J. Chem. Theory Comput.* **2012**, *8*, 4189-4203; (b) M. Renz, M. Kaupp, *J. Phys. Chem. A* **2012**, *116*, 10629-10637; (c) M. Kaupp, M. Renz, M. Parthey, M. Stolte, F. Würthner, C. Lambert, *Phys. Chem. Chem. Phys.* **2011**, *13*, 16973-16986; (d) M. Renz, K. Theilacker, C. Lambert, M. Kaupp, *J. Am. Chem. Soc.* **2009**, *131*, 16292-16302.

[11] (a) M. Kaupp, S. Gückel, M. Renz, S. Klawohn, K. Theilacker, M. Parthey, C. Lambert, *J. Comput. Chem.* **2016**, *37*, 93-102; (b) M. Parthey, K. B. Vincent, M. Renz, P. A. Schauer, D. S. Yufit, J. A. K. Howard, M. Kaupp, P. J. Low, *Inorg. Chem.* **2014**, *53*, 1544-1554; (c) M. Kaupp, A. Karton, F. A. Bischoff, *J. Chem. Theory Comput.* **2016**, *12*, 3796-3806.

[12] A. V. Arbuznikov, M. Kaupp, *J. Chem. Phys.* **2012**, *136*, 014111.

[13] (a) M. E. Smith, R. L. Cordiner, D. Albesa-Jove, D. S. Yufit, F. Hartl, J. A. K. Howard, P. J. Low, *Can. J. Chem.* **2006**, *84*, 154-163; (b) R. L. Cordiner, M. E. Smith, A. S. Batsanov, D. Albesa-Jove, F. Hartl, J. A. K. Howard, P. J. Low, *Inorg. Chim. Acta* **2006**, *359*, 946-961; (c) R. L. Cordiner, D. Corcoran, D. S. Yufit, A. E. Goeta, J. A. K. Howard, P. J. Low, *Dalton Trans.* **2003**, 3541-3549; (d) M. E. Smith, E. L. Flynn, M. A. Fox, A. Trottier, E. Wrede, D. S. Yufit, J. A. K. Howard, K. L. Ronayne, M. Towrie, A. W. Parker, F. Hartl, P. J. Low, *Chem. Commun.* **2008**, 5845-5847.

[14] W. Kaim, J. Fiedler, *Chem. Soc. Rev.* **2009**, *38*, 3373-3382.

[15] J. B. G. Gluyas, N. J. Brown, J. D. Farmer, P. J. Low, *Aust. J. Chem.* **2017**, *70*, 113-119.

[16] (a) D. M. D'Alessandro, F. R. Keene, *Dalton Trans.* **2004**, 3950-3954; (b) R. F. Winter, *Organometallics* **2014**, *33*, 4517-4536.

[17] N. G. Connelly, W. E. Geiger, *Chem. Rev.* **1996**, *96*, 877-910.

[18] M. Kaupp, *J. Comput. Chem.* **2007**, *28*, 320-325.
[19] E. C. Fitzgerald, N. J. Brown, R. Edge, M. Helliwell, H. N. Roberts, F. Tuna, A. Beeby, D. Collison, P. J. Low, M. W. Whiteley, *Organometallics* **2012**, *31*, 157-169.
[20] (a) E. C. Fitzgerald, A. Ladjarafi, N. J. Brown, D. Collison, K. Costuas, R. Edge, J. F. Halet, F. Justaud, P. J. Low, H. Meghezzi, T. Roisnel, M. W. Whiteley, C. Lapinte, *Organometallics* **2011**, *30*, 4180-4195; (b) A. Burgun, F. Gendron, C. J. Sumby, T. Roisnel, O. Cador, K. Costuas, J. F. Halet, M. I. Bruce, C. Lapinte, *Organometallics* **2014**, *33*, 2613-2627; (c) K. Costuas, O. Cador, F. Justaud, S. Le Stang, F. Paul, A. Monari, S. Evangelisti, L. Toupet, C. Lapinte, J. F. Halet, *Inorg. Chem.* **2011**, *50*, 12601-12622; (d) M. A. Fox, B. Le Guennic, R. L. Roberts, D. A. Brue, D. S. Yufit, J. A. K. Howard, G. Manca, J. F. Halet, F. Hartl, P. J. Low, *J. Am. Chem. Soc.* **2011**, *133*, 18433-18446.
[21] F. Paul, L. Toupet, J. Y. Thepot, K. Costuas, J.-F. Halet, C. Lapinte, *Organometallics* **2005**, *24*, 5464-5478.
[22] M. I. Bruce, C. Hameister, A. G. Swincer, R. C. Wallis, *Inorg. Synth.* **1982**, *21*, 78-84.
[23] S. Bock, S. G. Eaves, M. Parthey, M. Kaupp, B. Le Guennic, J. F. Halet, D. S. Yufit, J. A. K. Howard, P. J. Low, *Dalton Trans.* **2013**, *42*, 4240-4243.
[24] J. B. G. Gluyas, A. J. Boden, S. G. Eaves, H. Yu, P. J. Low, *Dalton Trans* **2014**, *43*, 6291-6294.
[25] G. R. Fulmer, A. J. M. Miller, N. H. Sherden, H. E. Gottlieb, A. Nudelman, B. M. Stoltz, J. E. Bercaw, K. I. Goldberg, *Organometallics* **2010**, *29*, 2176-2179.
[26] M. Krejcik, M. Danek, F. Hartl, *J. Electroanal. Chem.* **1991**, *317*, 179-187.
[27] (a) TURBOMOLE, V6.4 2012; TURBOMOLE GmbH: Karlsruhe, Germany; (b) TURBOMOLE, V7.1 2016; TURBOMOLE GmbH: Karlsruhe, Germany http://www.turbomole.com.
[28] (a) A. D. Becke, *Phys. Rev. A* **1988**, *38*, 3098-3100; (b) C. T. Lee, W. T. Yang, R. G. Parr, *Phys. Rev. B* **1988**, *37*, 785-789.
[29] M. Parthey, M. Kaupp, *Chem. Soc. Rev.* **2014**, *43*, 5067-5088.
[30] aA. Klamt, G. Schuurmann, *J Chem Soc Perk T 2* **1993**, 799-805; bA. Klamt, *Wires Comput Mol Sci* **2011**, *1*, 699-709.
[31] F. Weigend, R. Ahlrichs, *Phys Chem Chem Phys* **2005**, *7*, 3297-3305.
[32] S. Grimme, J. Antony, S. Ehrlich, H. Krieg, *J. Chem. Phys.* **2010**, *132*, 154104.
[33] K. Theilacker, A. V. Arbuznikov, M. Kaupp, *Mol. Phys.* **2016**, *114*, 1118-1127.

10.1002/chem.201901200

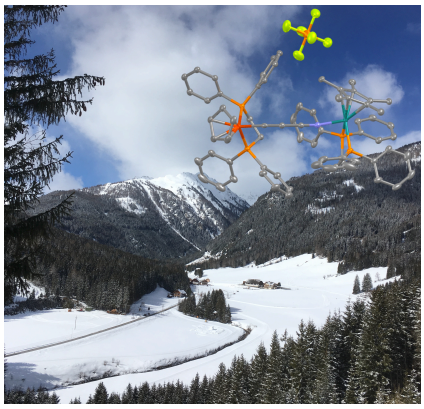

Mapping the landscape: Conformational mixtures of mixed-valence (MV) complexes are studied using a combination of NIR spectroscopy and DFT methods. Just three minima chosen the sample the potential energy hypersurface prove sufficient to describe the electronic structures and account for the IVCT bandshape.

Mixed-valence landscapes

S. Gückel, J.B.G. Gluyas, S.G. Eaves, P. Safari, D.S. Yufit, A.N. Sobolev, M. Kaupp, P.J. Low

A Combined Spectroscopic and Computationally 'Minimal' Approach to the Analysis of the Electronic Spectra and Electronic Structures of Mixed-Valence Complexes.